Trabajo de grado

(Proyecto de investigación)

Facultad de Ciencias Naturales y Exactas

Departamento de Física

Universidad del Valle

Study of doublon dynamics in optical lattices: spin chains and perspectives on quantum control

By:
Manuel Humberto Muñoz

Advisor:
Prof. Javier Madroñero Pabón

Co-advisor:
Dr. Carlos Alberto Parra Murillo

Santiago de Cali, Octubre 22 del 2015

To my parents.

Contents

Resumen

Motivados por los recientes experimentos en simulación cuántica y los avances en control coherente, ambos haciendo uso de gases cuánticos ulrafríos en redes ópticas, hemos estudiado temáticas particulares dentro de cada una de estas dos grandes áreas de la física cuántica moderna. Hemos dedicado la primer parte de esta tesis al estudio de modelos de magnetismo cuántico en una dimensión, especialmente la cadena XXZ, esto usando un modelo de Bose-Hubbard en la aproximación de una sola banda energética para bosones ultrafríos en una red óptica unidimensional. Establecimos una conexión entre el sistema atómico y el sistema magnético gracias a la propagación de una excitación, denominada dipolo (par ocupación doblón-hueco) del sistema atómico en el contexto de una red inclinada. En un segundo capítulo hemos explorado, con un modelo de Bose-Hubbard en la aproximación de dos bandas energéticas, la dinámica entre bandas que se puede establecer mediante la inclusión de un término que acople éstas a partir de ocupaciones dobles de los sitios de red en la banda inferior.

Abstract

Motivated by state-of-the-art experiments related to quantum simulation with ultra cold quantum gases and by the advances in the coherent control of ultracold matter, we theoretically address issues encircling two large areas of quantum physics: quantum simulation and coherent control. We devote the first chapter of this thesis to the study of one dimensional quantum magnetism, especially in the case of a XXZ Heisenberg model, by means of a single band Bose-Hubbard Hamiltonian. This research, based in the issue of ultracold quantum gases, clearly shows how the Feynmann's idea of quantum simulation works. As it will be shown a fundamental physical entity is the quasiparticle known as dipole, a pair of doublon-holon. A second chapter consider a similar type of dynamics but extending our model by including a second Bloch band to our Bose-Hubbard Hamiltonian. Here we explore possibilities of coherent control of the inter-band dynamics estrictly induced by the creation of doublons in the lowest energy Bloch band.

Chapter 1

Introduction

Since the beginning of quantum theory in the $1900's$ one of its major applications has been the study of matter. Nowadays we call it quantum matter and is one of the fields with the larger activity in both theory and experiment. The field had a boost with the development of modern techniques of cooling and trapping atoms that gave the Nobel prices in physics to Steven Shu, John Phillips and Cohen-Tannoudji in 1997, followed by the successful achievement of the Bose-Einstein condensation [1–3] that was recognized with the Nobel price of 2001 to Eric Cornell, Wolfgang Ketterle, and Carl Wieman. That gave birth to a field known today as ultracold matter or ultracold atoms physics, which has had great success thanks to the possibilities of trapping and controlling quantum matter. Perhaps the first experimental proof of this high controllability was realized by Greiner *et al.* in 2002 [4] by showing how a sample of Rubidium atoms loaded in an optical lattice can undergo a phase transition between superfluid and Mott-insulator phases, and the reversibility of the process. Since then there have been extensive developments in this field, many of those are summarized and can be found in [5].

Since ultracold atoms loaded in optical lattices present the most cleanest setup available today, physicists have taken advantage of this to study complex condensed matter systems in regimes that are usually unreachable. This thanks to the implementation of today-called quantum simulators [6–9]. In addition, it is possible to study quantum matter dynamically, where usually this evolution mixes a large number of accessible states and it results in diffusion in the large Hilbert space of the problem [10]. However the high controllability of ultracold matter has allowed physicists to propose and test protocols for the coherent control of the time evolution of quantum systems, see for example [11–13].

1.1 Quantum simulation

The high difficulty of studying quantum systems by means of the computational tools available today has open a whole new field in quantum physics: Quantum simulation: As Richard Feynman said “Nature is not classical, dammit, and if you want to make a simulation of nature, you would better make it quantum mechanical, and by golly it is a wonderful problem, because it does not look so easy” [14]. At the core of this field we found a simple idea. As Feynman said, you can mimic the behavior of a quantum system with another more controllable one. The main objective

of having a more controllable system is to extract useful information about the behavior of the original system, information that can otherwise be screened or destroyed by noise or the influence of impurities and defects when studying the original system.

Although quantum simulation is a nice and simple idea, its implementation is not an easy task. First, a good system to be used as quantum simulator has to be found. Fortunately, modern techniques of cooling and trapping atoms even at the level of single ions [6], perfected superconducting cavities [15], photonic crystals [16], quantum dot and quantum circuits [17] form a set of possibilities for a choice of which is the best suited quantum simulator.

In this work we explore quantum simulation of one dimensional spin chains. Among the different systems that can be used as quantum simulators we will focus our attention on trapped ultracold quantum gases, for which a high degree of controllability has been reached, and in fact they have already been used to simulate some complex quantum systems as the Hofstader Hamiltonian [8] and frustration in a spin system [9].

1.2 Ultracold atoms and optical lattices

Atomic systems cooled near to the absolute zero and periodic lattices made up by the superposition of counterpropagating laser beams offer one of the cleanest experimental setups we have today. The system is characterized by a high degree of control over the parameters of the systems, as was proven by the achievement of the Bose-Einstein condensation [1–3] and the phase transition between Mott insulator and superfluid states [4]. The possibilities for a system of ultracold atoms loaded in an optical lattice are huge. This can be seen from the active and dynamic growth this field has had over the last decade [5], and it has found its place in modern physics as an independent field of research rather than a branch of a larger field.

In the present section we want to introduce some basic notions related to ultracold atoms and optical lattices that are going to be helpful for understanding further developments presented in this thesis.

1.2.1 Bose-Einstein condensation

For many years the limit of how low the temperature of a sample can be reduced was placed at the temperature of liquid nitrogen. However, with the understanding of the statistical nature of temperature that barrier could be overcome. Nowadays we frequently hear of ultracold temperatures that goes up to hundredths of Kelvin's as near to the absolute zero as never before. All this thanks first to modern techniques of trapping matter as Magneto Optical Traps (MOT), optical lattices, or optical molasses. And some modern cooling techniques as Doppler cooling [18, 19], Sisyphus cooling (see Sec. 8.8 in [20]), and evaporative cooling [21]. The temperatures that have been reached with these techniques have been low enough to achieve and observe some exotic and novel phenomena. For example, Bose-Einstein condensation (BEC) [1–3] which occurs around 10^{-5} K in diluted gases, though this temperature depends on the confinement potential (chapter 1 of [22]).

As predicted by Bose and Einstein [23], a collection of bosons cooled near the absolute zero

undergoes a phase transition characterized by a massive occupation of one quantum state. This can be seen either from the singularity that appears in the occupation number when described by Bose-Einstein statistics, or when one or more eigenvalues $n_i(t)$ of the reduced single-particle density matrix is of the order of the total number of particles N

$$\rho(\boldsymbol{r}\alpha, \boldsymbol{r}'\alpha'; t) \equiv \langle \hat{\phi}^\dagger(\boldsymbol{r}, \alpha)\hat{\phi}(\boldsymbol{r}', \alpha')\rangle = \sum_i n_i(t)\chi_i^*(\boldsymbol{r}, \alpha; t)\chi_i(\boldsymbol{r}', \alpha'; t)\,, \tag{1.1}$$

where $\hat{\phi}(\boldsymbol{r}, \alpha)$ represents bosonic field operators, with α denoting additional degrees of freedom, and $\chi_i(\boldsymbol{r}, \alpha; t)$ are single particle eigenfunctions of $\rho(\boldsymbol{r}\alpha, \boldsymbol{r}'\alpha'; t)$. Although BEC is not the main subject of the present work it helps us to understand up to what extend ultracold temperatures have allowed physics to advance in the study of quantum matter.

1.2.2 Optical lattices

An optical lattice can be understood as a periodic chain of atomic traps or potential wells in which atoms can be confined due to the interaction between their atomic dipolar momentum and the electric field. Periodic potentials are generated by the interference of counter-propagating laser beams, where the resulting standing wave has a period equal to $\lambda/2$ with λ the wavelength of the used laser. If the electric field of the laser varies spatially, then it generates an electric force on the atoms [24]

$$\boldsymbol{F}_{\text{dip}} = \frac{1}{2}\alpha(\omega_L)\nabla\left[|\boldsymbol{E}(\boldsymbol{r})|^2\right]\,, \tag{1.2}$$

where $\alpha(\omega_L)$ is the atomic polarizability and ω_L is the field frequency. The interaction with the electric field makes the atoms experience a dipole potential given by [24]

$$V_{\text{dip}}(\boldsymbol{r}) = \frac{3\pi c^2}{2\omega_0^3}\frac{\Gamma}{\Delta}\langle|\boldsymbol{E}(\boldsymbol{r})|^2\rangle\,, \tag{1.3}$$

with $\Delta = \omega_L - \omega_0$ the detuning between the frequency of the field and the atomic transition frequency ω_0. In the semi-classical treatment (particles are quantized and the radiation is treated classically), the atom is treated as a two level system with decay rate Γ. An optical potential exerts a repulsive force on the atoms if we have blue detuning $\Delta > 0$ and an attractive one if we have red detuning $\Delta < 0$ [5]. Periodic potentials in 2D and 3D can be realized by including extra pairs of counterpropagating laser beams and varying the angles between the pairs, typically those angles are set such that the pairs are orthogonal. Here, we are interested in a one dimensional profile created by the interference of two laser beams one with half the periodicity of the other. Thus, our dipole potential reads

$$V_{\text{dip}}(\boldsymbol{r}) = -V_0[\cos(2k_L x) + s_0\cos(4k_L x + \phi)]\,, \tag{1.4}$$

with $s_0 = \frac{V_1}{V_0}$ and ϕ the phase difference between the two cosinusoidal waves of amplitudes V_0 and V_1, respectively. With this potential profile we can effectively isolate the first two Bloch bands, that is, eigenenergy bands of a free particle in a periodic potential, and thus neglect the influence of higher bands on the system. Usually this set up is called a bichromatic potential or miniband structure, and its properties can be controlled by means of the parameters s_0 and ϕ [25]. In addition we can introduce an external field $V_{\text{WS}}(x) = Fx$ to define the known Wannier-Stark system [26].

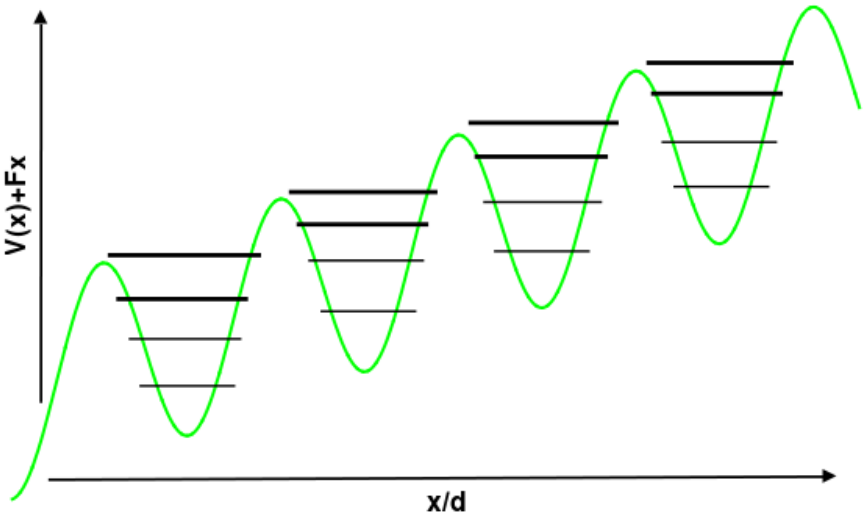

Figure 1.1: Schematic representation of a Wannier-Stark ladder in a monochromatic potential, including the first and second energy bands, the extra levels correspond to the raising in each band energy when there is more than one particle in a site. With $d = d_L$.

1.3 The Wannier-Stark system

1.3.1 Generalities

As mentioned in Sec. 1.2.2 by introducing an external field of the form $V_{\mathrm{WS}}(x) = Fx$, we obtain the Wannier-Stark system. The Hamiltonian for the tilted lattice reads

$$\hat{H}_0 = -\frac{\hbar^2}{2m_0}\frac{\partial^2}{\partial x^2} + V(x) + Fx, \qquad \text{with} \qquad V(x + d_L) = V(x)\,, \tag{1.5}$$

where F is a static external force that can be treated as a control parameter. The energies of the system are given by $\epsilon_l = E_0 + l d_L F$ [27], that is, the energies are obtained after translation over l wells of the lattice starting from the untilted system energy E_0 (see Fig. 1.1). On the other hand, the eigenstates of the system, commonly known as Wannier-Stark states are given by

$$|w_l\rangle = \sum_m J_{m-l}\left(\frac{J}{2d_L F}\right)\hat{a}_m^\dagger|0\rangle\,, \tag{1.6}$$

where J_{m-l} is a Bessel function of the first kind, and d_L is site separation distance or lattice constant. These states are localized functions in the coordinate space at the lth well of the lattice. Schematically, in presence of a fixed force, the energy levels of the Wannier-Stark system represent a set of equidistant states, called the Wannier-Stark ladder. For every energy band one can build the respective Wannier-Stark ladder and they are going to be separated by an energy gap, say $\Delta_{\beta\beta'}$ which varies as we go up in the band index β. The Hamiltonian in Eq. (1.5) is unbounded and with a continuum spectrum, *i.e.*, it does not have discrete eigenvalues [26]. Such contradiction finds its solution in the following argument, the spectrum is complex and the discrete

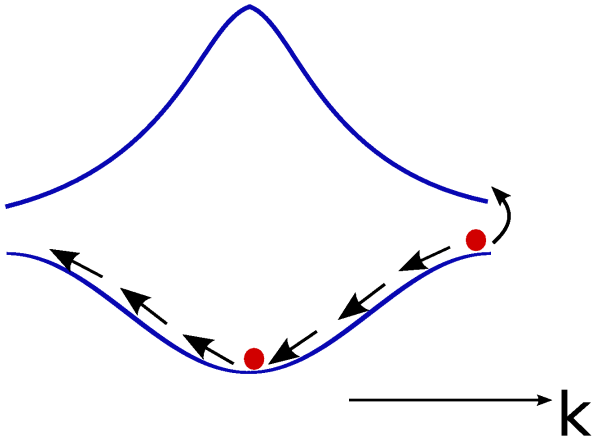

Figure 1.2: Schematic representation of the two main processes taking place in the Wannier-Stark system. Bloch oscillations within the first Brillouin zone and Landau-Zener tunneling to higher bands [26].

energies presented above are resonances embedded in the complex continuum

$$\epsilon_l^\beta = E_\beta + l d_L F - i\frac{\Gamma_\beta}{2}\,, \tag{1.7}$$

where Γ_β stands for the decay rate of each band that appears as a consequence of the unbounded spectrum and the Wannier-Stark states being metatestable. Among the effects that arises as consequences of the external force, Bloch oscillations [28] are one of the most interesting. When we place a particle on a given lattice site it will get accelerated but without escaping from the lattice confinement. Instead it will undergoes Bloch oscillations with a period $T_B = 2\pi\hbar/d_L F$, known as the Bloch period. The other interesting process is Landau-Zener tunneling characterized by the promotion of particles lying in the lower band to higher energy bands, as we can see in Fig. 1.2: when the particle is undergoing Bloch oscillations there is a non-zero probability for it to get promoted to the upper band as it gets closer to the boundary of the first Brillouin zone. This effect gets naturally enhanced when two different Wannier-Stark ladders get maximally coupled via interband resonant tunneling at values of the force approximately given by

$$F_{|l-l'|} \approx \frac{\Delta_{\beta,\beta'}}{d_L|l-l'|}\,, \tag{1.8}$$

where $\Delta_{\beta,\beta'}$ is the energy separation between Bloch bands β, β', and l, l' are the lattice sites whose lower(upper) and upper(lower) single particle levels become degenerate respectively. Following the notation of ref [29], we define $r = |l - l'|$ as the order of the resonance with $r \in \mathbb{Z}$. In the following, the vicinity of the Stark force F_r will be referred as the resonant regime.

1.4 The Bose-Hubbard model

In this work we will be dealing mainly with the single-band Bose-Hubbard model. However, here we are going to present some short passage on the derivation of the whole model for the many body problem (a more complete treatment can be found in chapter 3 of [30]). To do so, the general

Hamiltonian we need to study is [31],

$$H = \int \hat{\phi}^\dagger(x)[H_0(x) + Fx]\hat{\phi}(x)\mathrm{d}x + g_{1D}\int\int \hat{\phi}^\dagger(x)\hat{\phi}^\dagger(x)\delta(x-x')\hat{\phi}(x')\hat{\phi}(x')\mathrm{d}x\mathrm{d}x'\,, \quad (1.9)$$

where the second term stands for the allowed interaction between particles, which is reduced only to contact ones described by a pseudo-potential $g_{1D}\delta(x)$ [32]. In order to compute the transformation of each of the terms in Eq. (1.9) we need to define the proper field operators for our description. These operators can be defined in the following way. It is known that the periodic problem has its solution in the Bloch theorem, therefore $\psi_k^\alpha(x) = e^{ikx}u_k^\alpha(x)$ known as Bloch waves are solutions of

$$H_0\psi_k^\alpha(x) = E_k^\alpha\psi_k^\alpha(x), \qquad \text{with} \qquad H_0(x) = \frac{P^2}{2m} + V_0\cos(2k_Lx), \quad (1.10)$$

where k represents the quasi-momentum restricted to first Brillouin zone $-\pi/d_L \leq k \leq \pi/d_L$, α labels the band, and $u_k^\alpha(x)$ are functions with the same period as the lattice $u_k^\alpha(x+d_L) = u_k^\alpha(x)$. Here E_k^α are the eigenenergies, the so-called Bloch energy bands since k is continuous. Since the Bloch waves are periodic functions of the quasimomentum they can be expanded in a Fourier series. The expansion can be written as

$$\psi_k^\alpha(x) = \sqrt{\frac{d_L}{2\pi}}\sum_{x_l} w^\alpha(x-x_l)e^{ikx_l},$$

$$\text{with expansion coefficients} \qquad w^\alpha(x-x_l) = \sqrt{\frac{d_L}{2\pi}}\int_{BZ}\psi_k^\alpha(x)e^{-ikx_l}\mathrm{d}x\,, \quad (1.11)$$

where the expansion coefficients are the known Wannier Functions [33]. In Eq. (1.11) $x_l = d_Ll$ and l labels the lattice site. Some properties of the wannier functions are that they form an orthonormal set, and their parity is band dependent as follows

$$\int w^\alpha(x-x_l)w^{\alpha'}(x-x_l') = \delta_{\alpha\alpha'}\delta_{ll'}, \quad (1.12)$$

$$w^\alpha(-x) = (-1)^{\alpha-1}w^\alpha(x)\,. \quad (1.13)$$

The maximal localized Wannier functions that drop exponentially for $x < |d_L|$ [34] can be obtained once we have guaranteed the analyticity of the Bloch waves (for a deeper discussion on Bloch and Wannier functions see App. 1 of [35]). We write the field operators in terms of the Wannier functions to obtain a description of local single-particle states,

$$\hat{\phi}(x) = \sum_{\alpha=1}^{\infty}\sum_{l\in\mathbb{Z}} w^\alpha(x-x_l)\hat{a}_l^\alpha, \quad (1.14)$$

where the operator $\hat{a}_l^{\alpha\dagger}$ creates a boson in well l on band α. For short, we will speak site l and band α.

In the following and throughout this work we set $\hbar = 1$ and the energy unit is given by the recoil energy $E_r = k_L^2/2m$. Additionally, we use the rescaling

$$k \to k/k_L, \quad x \to x/d_L, \quad V_i \to V_i/E_r\,. \quad (1.15)$$

Now that we have a clear definition of the field operators we can proceed by writing down the explicit form of each of the terms in Eq. (1.9). The part corresponding to the periodic problem reads

$$\int \hat{\phi}^\dagger(x)[H_0(x)\hat{\phi}(x)]\mathrm{d}x = \sum_\alpha \sum_{l,l'} J^\alpha_{l-l'} \hat{a}^{\alpha\dagger}_l \hat{a}^\alpha_{l'},$$

$$\text{with} \qquad J^\alpha_{l-l'} \equiv \int w^\alpha(x-x_l) H_0(x) w^\alpha(x-x_{l'})\mathrm{d}x = \epsilon^\alpha_{l-l'}, \quad (1.16)$$

where $\epsilon^\alpha_{l-l'}$ represents the Fourier transformation of the eigenenergies. Here the contribution mediated by $J^\alpha_{l-l'}$ is referred as hopping because it destroys a particle in a site l and creates it on a site l'. Although there is a possibility for hopping between different bands by computing an expansion of the Bloch hamiltonian in terms of the creation (annihilation) operators, the coefficients for such transitions are zero due to the orthonormality of the Wannier functions (see Chap. 3 of [30]).

The term containing the external Stark force transforms under the field operators defined in Eq. (1.14) as

$$F\int \hat{\phi}^\dagger(x)\, x\, \hat{\phi}(x)\mathrm{d}x = d_L F \sum_{\alpha,l} l\, \hat{a}^{\alpha\dagger}_l \hat{a}_l + d_L F \sum_{\alpha,\alpha'}\sum_{l,l'} C^{\alpha\alpha'}_{l-l'} \hat{a}^{\alpha\dagger}_l \hat{a}^{\alpha'}_{l'},$$

$$\text{where} \qquad C^{\alpha\alpha'}_{l-l'} \equiv \int w^\alpha(x-x_l) x w^{\alpha'}(x-x'_l)\mathrm{d}x\,. \quad (1.17)$$

We see that the external field has the following effects: first it tilts the lattice, and second it couples different sites and bands. Here, the parity property in Eq. (1.12) implies that the external force does not couple different sites in the same band. Finally, the term of the interparticle interaction in Eq. (1.9) takes the form

$$g_{1D}\int \hat{\phi}^\dagger(x)\hat{\phi}^\dagger(x)\hat{\phi}(x)\hat{\phi}(x)\mathrm{d}x = \sum_{\alpha_1,\ldots,\alpha_4}\sum_{l_1,\ldots,l_4} M^{\alpha_1\ldots\alpha_4}_{l1\ldots l_4} \hat{a}^{\alpha_1}_{l_1}\hat{a}^{\alpha_2}_{l_2}\hat{a}^{\alpha_3}_{l_3}\hat{a}^{\alpha_4}_{l_4},$$

$$\text{with} \qquad M^{\alpha_1\ldots\alpha_4}_{l1\ldots l_4} \equiv g_{1D}\int w^{\alpha_1}(x-x_l)w^{\alpha_2}(x-x_l)w^{\alpha_3}(x-x_l)w^{\alpha_4}(x-x_l)\mathrm{d}x\,. \quad (1.18)$$

Since the Wannier functions are maximally localized on the lattice sites the dominant contributions to the interaction are on-site ones given by $M^{\alpha_1\ldots\alpha_4}_{llll}$. However, the parity of the Wannier functions force many of these coefficients to vanish. A more broad discussion on the Bose-Hubbard coefficients can be found in Chap. 1 of [36].

As stated at the beginning of this section our main object of study is the single-band Bose-Hubbard Hamiltonian. This model is a reduction of the full many-body problem presented here when we truncate the number of energy bands to one, and in terms of the previous expressions it reads,

$$H = \sum_{l,l'} J_{l-l'} \hat{a}^\dagger_l \hat{a}_{l'} + d_L F \sum_l l \hat{a}^\dagger_l \hat{a}_l + \sum_l M^{1111}_{llll} \hat{a}^\dagger_l \hat{a}^\dagger_l \hat{a}_l \hat{a}_l, \quad (1.19)$$

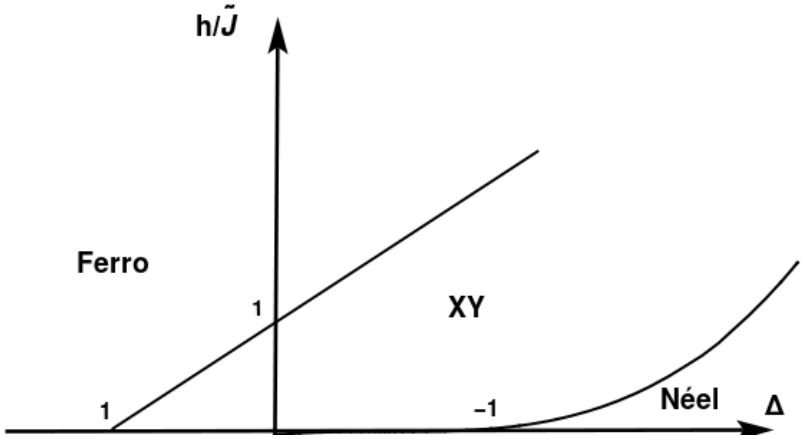

Figure 1.3: Phase diagram of the XXZ-model for $S = 1/2$ in presence of an external field in z-direction [37].

1.5 Some properties of the XXZ-chain model

The study of one-dimensional quantum magnetism is one of the more prolific areas in condensed matter physics. Both, because it provides physicists with a better understanding of strong correlated systems and because it has direct application on the study of real materials. One paradigmatic model in the study of these quantum systems is known as the Heisenberg XXZ-chain model. This model features two different phases. The ferromagnetic phase and the anti-ferromagnetic phase or Néel phase.

Here, we have special interest in a $S = 1/2$ XXZ chain in presence of an external field in the z-direction. The specific Hamiltonian reads

$$H = \tilde{J} \sum_n (\sigma_n^x \sigma_{n+1}^x + \sigma_n^y \sigma_{n+1}^y + \Delta \sigma_n^z \sigma_{n+1}^z) + h \sum_n \sigma_n^z \,, \tag{1.20}$$

where σ_n^i, $i = x, y, z$ are the usual Pauli matrices, $\tilde{J}$ the super exchange coupling, Δ the anisotropy parameter, and h the strength of the magnetic field. Additionally, the most important feature of this model is that the longitudinal coupling between spins interchanges up and down spins, $|\uparrow\downarrow\rangle \rightarrow |\downarrow\uparrow\rangle$. This coherent exchange of the positions of two spins in adjacent sites is known as superexchange (see [37]).

The phase diagram of the XXZ-Heisenberg model in presence of a z-external Zeeman field can be viewed in Fig. 1.3, where the regions for each of the three main phases, ferromagnet, antiferromagnet and XY are delimited. A more deep presentation of this phase diagram can be found in [38].

We have special interest in the two opposed phases of the model, both presented in Fig. 1.3. The ferromagnetic phase appears for $\Delta < -1$. In this phase the XXZ chain exhibits a ground state where all spins point either up or down, with total magnetization different from zero. The introduction of the external Zeeman field does not alter the system because the total spin component σ_{tot}^z commutes with the Hamiltonian leading only to an increment in the energy without

altering the wave functions. However, it does stabilize the ground state and lift the broken spin inversion symmetry. Here the basic excitations of the ground state are called magnons. They are single impurities that breaks the large order of the ferromagnet and can, as a consequence of the superexchange, travel along the chain.

The Néel or antiferromagnetic phase appears for $\Delta > 1$. This face features, in the thermodinamic limit, a two-fold degenerated ground state with zero total magnetization but finite sublattice magnetization, $N^z = \sum_n (-1)^n \sigma_n^z$. In contrast with the Ferromagnetic phase quantum fluctuations prevent the order from being complete since the sublattice magnetization does not commute with the XXZ Hamiltonian.

The excitations of these phase can be understand thinking on the ground states at the thermodynamic limit. One starts there from either of the two degenerated ground states and breaks only one bond one will end up with a cluster of three spins oriented in the same fashion. Later the superexchange will change this configuration by another one where the cluster has recovered its alternating order but on each side of the cluster there will be two small clusters of two spins oriented in the same fashion. These are known as two-domain walls and as for the magnons in the ferromagnet they can propagate along the chain. One can see that for a finite system depending on how many bonds you break in the antiferromagnetic ground state you could arrive to a similar state where a single spin impurity propagates.

There is an additional phase that lies just in the middle of the two previously mentioned phases. However, for the sake of keeping the discussion in this thesis simple and related to what will be presented in incoming chapters we are not dealing with the XY phase here. Nevertheless we recommend [37] for the interested reader.

1.6 The rest of this work

In Chap. 1 we presented some necessary concepts for the later developments of this work. Mainly, they are ultracold atoms and optical lattices in Sec. 1.2, the one-dimensional Bose-Hubbard model in Sec. 1.4, and the Heisenberg XXZ-chain model in Sec. 1.5. The subsequent chapters are devoted to the study of two main areas. First, quantum simulation, in particular the construction of bridges between one dimensional ultracold atomic systems and one dimensional magnetism. Second, coherent control, taking advantage of the controllability of ultracold atomic systems to propose and test routes towards the achievement of a some states of interest. To do that the rest of this work is divided as follows.

In Chap. 2 we present one already proposed and tested quantum simulation of the antiferromagnetic Ising chain in transverse and longitudinal fields, and the link between second order processes in the single-band Bose-Hubbard model and spin transport in the form of spin waves in the Heisenberg XXZ-model. Later, in Chap. 3 we introduced the two-band Bose-Hubbard Hamiltonian with a doublon-mediated interband coupling, and the respective dynamical study was done using two different techniques, shaking the lattice and parametric evolution. All this looking forward to the achievement of some specific states. We include three appendices. App. A deals with some generalities of the Schrieffer-Wolff transformation and its application to the models studied in the two core chapters of this thesis. App. B presents a collection of results from Chap. 3 with the parametric evolution. App. C presents two different issues: In Sec. C.1 a more extensive ex-

planation of the procedure we used to study the interference time in Chap. 2 is presented, and in Sec. C.2 the situation of having an initial state with a dipole in the middle of the lattice is studied.

Chapter 2

Quantum simulation with the single-band Bose-Hubbard model

2.1 From the single-band Bose-Hubbard model to a Ising chain

One big question that arises when you want to simulate a spin system with bosons is how to restrict the otherwise large number of degrees of freedom allowed to bosonic particles. To find the proper regime in which the Hilbert spaces of the spin system and the bosonic system have commensurable dimensions is usually a hard task. However, it has been shown [39] and proven experimentally [7] that in the single band approximation of the Bose-Hubbard model, as presented in the previous chapter (Eq. (1.19)), it is indeed possible to find a proper regime in which the situation mentioned above occurs for the spin and bosonic systems. In the following sections we will present this regime and the quantum simulation that can be built working on it.

2.1.1 Mott insulator in a strong tilted lattice

The single-band Bose-Hubbard model was presented in Eq. (1.19). This model features two phenomenologically distinct phases, a superfluid one and an insulator one referred to as Mott insulator. This phase features negligible hopping amplitude (which translates to deep potential wells) and a definite average density of particles, with the site occupation number fixed. This is the phase we have interest to work with in the present chapter.

Our study is based on the B-H Hamiltonian but written in a slightly different form, where the operators accounting for the interaction part are written such that they stand for the double occupation of individual lattice sites. Such Hamiltonian reads

$$\hat{H} = -J \sum_{l} (\hat{a}_{l+1}^{\dagger} \hat{a}_l + \text{h.c.}) + \frac{U}{2} \sum_{l} \hat{n}_l (\hat{n}_l - 1) + F \sum_{l} l \hat{n}_l \,, \tag{2.1}$$

where J is the hopping amplitude between next neighboring sites, U is the interparticle energy interaction, F is the strength of the external field, $\hat{a}_l^{\dagger}$ ($\hat{a}_l$) are bosonic creation (annihilation) operators, and $\hat{n}$ is the boson number operator. In particular, we set $d_L = 1$. Usually the dynamics of this Hamiltonian is rather complex and can lead to chaotic behavior [30].

Here we are interested in the strong Stark forces regime and by that we mean

$$J, \quad |U - E| \ll U, \quad E\,. \tag{2.2}$$

We will focus our study in a initial state given by a Mott insulator with unitary filling ($n_0 = 1$), that is, we will work with deep wells such that $U \gg J$ and a mean density of particles per well equal to one. In other words the filling factor N/L (number of particles over number of sites) is going to be fixed at one. Even though we are in presence of a strong external field the Mott phase is stable [39]. The stability of the Mott state under the presence of the tilt is justified as long as the transition between untilted system and the tilted one is done via a sudden quench. In this case we can energetically lock the Mott state regardless the presence of the tilt.

In the strong Stark forces regime we basically tunned the external force to a point in which it is comparable with the energy given by the interparticle interaction. In other words the external force is bringing the energy level of a site into an energy degeneracy with the energy level of two particles in a next neighboring site. Then, the large Hilbert space of our problem can be effectively reduced to a manifold of states that are resonantly coupled to the Mott state. The reduction is way advantageous and we can see it from the calculation of the dimension of the Hilbert space for the resonant manifold given by,

$$\dim(H_{n+1}) = \dim(H_n) + \dim(H_{n-1}), \qquad \text{with} \quad \dim(H_1) = 1, \quad \text{and} \quad \dim(H_2) = 3\,, \tag{2.3}$$

where n stands for the number of lattice sites. This expression can be figured out by thinking on the number of different resonant states available from the Mott state for unitary filled lattices ($N/L = 1$) of length $L = 1, 2, 3, ...$ with periodic boundary conditions. We have to remember that the expression presented in Eq. (2.3) works only for the case of unitary filling.

The states that belong to the resonant manifold are accessible from the Mott state by means of a resonant transition [39, 40]. Those states given by the movement of a particle from one site to the next neighboring site when the energy levels of a single particle and two particles respectively are degenerated due to the external force. In Fig. 2.1 we present an example of such a transition. These resonant transitions are called dipole transitions, because in the process we have created a pair holon-doublon (a vacancy and two particles in next neighboring sites) as a consequence of the resonance. These dipoles are the only allowed deformations of the Mott state in our regime of interest [39] and together they constitute a good subspace of accessible states of our system.

The restriction on having further transitions once we have created the dipole is given by the fact that the external force does not couple the energy level of two particles with any other energy level in the direction of the tilt. Hence, we can treat the dipole as a whole entity in itself. To write an effective Hamiltonian it is convenient to introduce an operator that stands for the process of create or destroy a dipole. We define it as

$$\hat{d}_l^\dagger = \frac{\hat{a}_{l+1}^\dagger \hat{a}_l}{\sqrt{n_0(n_0+1)}}\,, \tag{2.4}$$

where n_0 is the average occupation that we set to one [39]. By introducing this operators we have reduced our problem to work in the subspace of dipole states and in such a scenario we can write

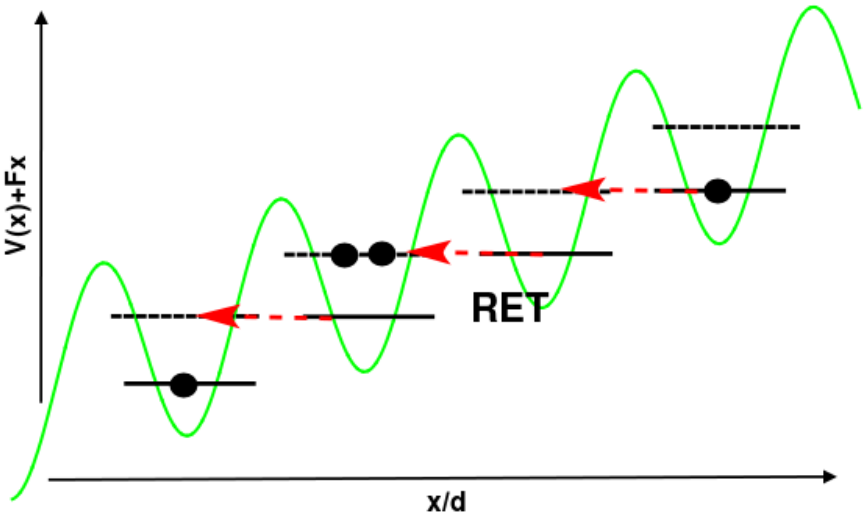

Figure 2.1: Schematic representation of a resonant transition as a consequence of the strong Stark force bringing close in energy the levels of a single particle (solid line) and two particles (dashed line) in next neighboring sites, such transitions happened usually at $U \approx E$. This process is known as resonant enhance tunneling (RET). With $d = d_L$.

an effective Hamiltonian for the Bose-Hubbard model in Eq. (2.1). It reads

$$\hat{H}_{\rm d} = -J\sqrt{2}\sum_l (\hat{d}_l^\dagger + \hat{d}_l) + (U-E)\sum_l \hat{d}_l^\dagger \hat{d}_l \,, \tag{2.5}$$

where we can either create or destroy a dipole with an amplitude J and once we have created it, it will have an energy $U - E$. We may notice that a single site of the lattice can support only one dipole and once we have a dipole in a given site we cannot create a dipole in the next neighboring site. Therefore, the Hamiltonian in Eq. (2.5) has the following restrictions:

$$\hat{d}_l^\dagger \hat{d}_l \leq 1 \qquad \text{and} \qquad \hat{d}_{l+1}^\dagger \hat{d}_{l+1} \hat{d}_l^\dagger \hat{d}_l = 0 \,. \tag{2.6}$$

The reduction of the Hilbert space of our system to the dipole subspace and the restrictions in Eq. (2.6) will allow us to build a spin chain simulator.

2.1.2 Antiferromagnetic Ising model in transverse and longitudinal fields

From the restrictions on the process of dipole creation we can extract the following information: (1) the number of dipoles per site is either one or zero. Therefore, this can be related to a system with two occupation values that can be understood in terms of spins. (2) The second restriction is reminiscent of a next neighboring interaction, since we cannot have dipoles in next neighboring sites. With this two statements in mind we define the following mapping between dipoles and spins:

$$\sigma_l^z = 1 - 2\hat{d}_l^\dagger \hat{d}_l, \qquad \sigma_l^x = \hat{d}_l^\dagger + \hat{d}_l, \qquad \text{and} \qquad \sigma_l^y = i(\hat{d}_l^\dagger - \hat{d}_l) \,. \tag{2.7}$$

An schematic representation of the spin mapping is presented in Fig. 2.2.

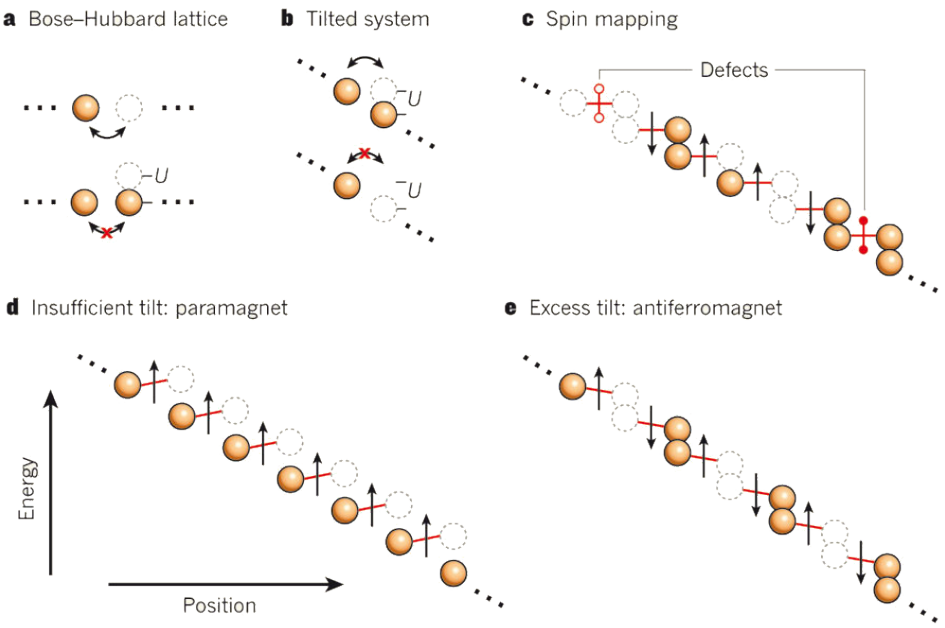

Figure 2.2: (a) Schematic representation of the different processes that take place within the single-band Bose-Hubbard model. (b) Representation of the allowed processes for the tilted single band system. (c) Spin mapping. (d) and (e) Two different phases exhibited by the Ising model in transverse and longitudinal field Eq. (2.8); for insufficient tilt (d) we have a paramagnetic phase and for excess of tilt (e) we have an antiferromagnetic phase [41].

We can thus write our dipole Hamiltonian in terms of spin operators, but for that it is useful to implement the constraint forbidding dipoles in next neighboring sites in the Hamiltonian such that we will have a next neighbor interaction. To do that we will include an energy term of the form $W\hat{d}^\dagger_{l+1}\hat{d}_{l+1}\hat{d}^\dagger_l\hat{d}_l = \frac{W}{4}(1-2\sigma^z_l+\sigma^z_{l+1}\sigma^z_l)$. After some algebra the Hamiltonian can be brought into the following form in terms of spin operators:

$$\hat{H}_{\rm s} = \tilde{W}\sum_l\left(\frac{1}{2}\sigma^z_{l+1}\sigma^z_l - h_x\sigma^x_l - h_z\sigma^z_l\right)\,. \tag{2.8}$$

This model is usually referred to as the Ising model in a transverse and longitudinal fields [42]. Here, $h_x = 2\sqrt{2}\frac{J}{W}$ and $h_z = 1-\frac{\Delta}{W}$, with $\Delta = E-U$, are the strengths of the longitudinal and transverse fields, respectively, and $\tilde{W} = \frac{W}{2}$. It is known that the interplay between the magnitude of the two fields drives a phase transition between a paramagnetic phase and an antiferromagnetic phase. Interestingly this phase transition can be in general classified as a second order phase transition [42]. However, there is a special point (multi critical point) at which the phase transition is a first order one. This is precisely the point where the parameters h_x, h_z and Δ take the values given above. That means, our simulation works precisely at the critical point [7].

To see a little bit clearer how the simulation we have presented in the last and present sections works, let us take a look at the dipole Hamiltonian, but first we define a control parameter given

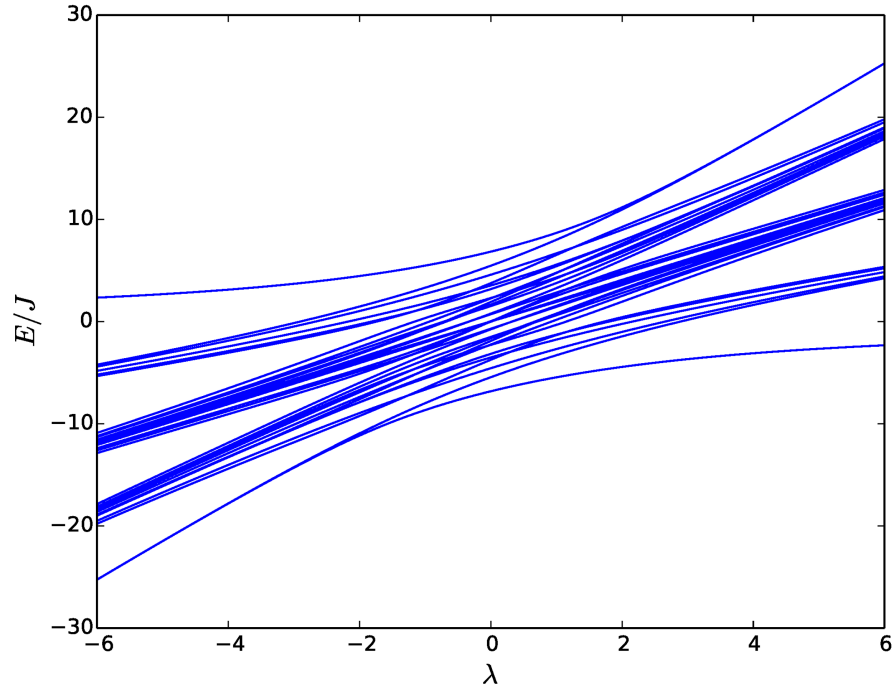

Figure 2.3: Energy spectrum for a chain with eight sites and unitary filled as a function of λ. We can see that the ground state exhibits two different behaviors, one for $\lambda \ll 1$ and for $\lambda \gg 1$, that we relate with a paramagnetic phase and an antiferromagnetic phase of the spins model. Here the dimension of the Hilbert space is $\dim(\hat{H}) = 47$.

by $\lambda = \frac{U-E}{J}$ that varies continuously. With that change the Hamiltonian now reads

$$\hat{H}_{\mathrm{d}} = -\sqrt{2}\sum_{l}(\hat{d}_l^{\dagger} + \hat{d}_l) + \lambda \sum_{l} \hat{d}_l^{\dagger}\hat{d}_l \,. \tag{2.9}$$

The explicit λ dependence of this Hamiltonian allows us to apply the definition of quantum phase transition given in [43]. In Fig. 2.3 we have computed the spectrum of the Hamiltonian in Eq. (2.9) for a chain of eight sites and unitary filling as a function of λ. If we focus our attention to the ground state we see that it exhibits two different behaviors (for further details see [43]). For $\lambda \gg 1$ the system is in a state with no dipoles and one particle per site, which corresponds to a paramagnetic phase according to the mapping presented in Fig. 2.2. For values of $\lambda \ll 1$ the ground state is two-fold degenerated, where these states are one with dipoles in every odd site and one with dipoles in every even site. Either of them corresponds to an antiferromagnetic phase, hence we can see that as we vary λ by changing the external force we drive the system from a paramagnet to an antiferromagnet.

The quantum simulation we have just presented was verified experimentally in 2011 in Greiner's ultracold atoms laboratory at Harvard University [7]. There, they could observe the transition from a paramagnet to an antiferromagnet and backwards as they ramp up and down the magnitude of the external field. For some clarifying comments on the methods implemented in [7] we recommend [41].

2.2 Signatures of spin-waves and interference in the single-band B-H model

In Sec. 2.1.2 we saw how it is possible to map a Bose-Hubbard model to a Quantum Ising chain in presence of both transverse and longitudinal fields. That was done by taking advantage of the natural resonant excitations of the Mott state once we energetically lock it in the tilted system. However, we have not provided further insights on this excitations. The objective of the present section is to explore the dynamics of those excitations.

As we have seen those excitations are a pair of holon-doublon called dipoles [39]. The first fact that was known is that dipoles are a whole structure on itself and they can move as such [39]. Therefore, a natural question that arises is whether one can have propagation of such an excitation when starting from a state with one dipole on one edge. Besides the time evolution of the system, the incoming sections are focused on the study of the particular situation outlined above when open boundary conditions are taken into account.

2.2.1 Second order processes in the single-band B-H model

As stated above we performed the time evolution of our system with an initial condition given by $|11...1120\rangle$, where the lattice was tilted upwards ($F > 0$), and far from any resonance. We take $F = xU + \delta$, where $x \in [3, 4)$, and δ a proper offset to guarantee that the system was outside of any kind of resonance. This last constraint was imposed in order to look for phenomena not considered so far in this work (notice that the case $F \approx U$ was studied in Sec. 2.1). In Fig. 2.4 we have plotted the population along the lattices sites, $\langle \hat{n}_l \rangle = \langle \psi(t) | \hat{n}_l | \psi(t) \rangle$, for the time evolution performed.

All the simulations where performed for different sets of Bose-Hubbard parameters. In particular the results presented in this section were obtained with the parameters of [44]. Regarding the range of values we have chosen for x it was a range where we are away of the situation presented in Sec. 2.1 and with a not to large tilt such that the wells were completely isolated one from another.

From Fig. 2.4 we can see that the time evolution has two major characteristics. First, it allows the dipole to propagate all along the lattice, though the initial information about the localization of it is not completely preserved through the propagation. Second, once the dipole has completed one transit it starts to propagate backwards but before completing the second transit it interferes with itself. That manifested itself as the splitting of the probability distribution of single site occupation, as can be seen in Fig. 2.4. This sort of behavior can be linked to the so called quantum carpets [45]. The link is more easily done in the limit of lattices with a large number of sites (as we will see in Sec. 2.2.4). Let us talk first about the dipole propagation. If we take a look to the Bose-Hubbard Hamiltonian in Eq. (2.1) it is easy to see that this model does not allow transport of particles beyond hopping and resonant tunneling. However, we are seeing that the dipole as whole jumps from one site to the next-neighboring one and so on until it has reach the opposite edge of the chain. Actually it evolves as $|111120\rangle \rightarrow |111201\rangle \rightarrow |112011\rangle \rightarrow |120111\rangle \rightarrow |201111\rangle$. Here the movement of the dipole can only be realized by two successive hoppings. Hence, we have a second order tunneling process. At this point one can be wondering, how to extract the relevant

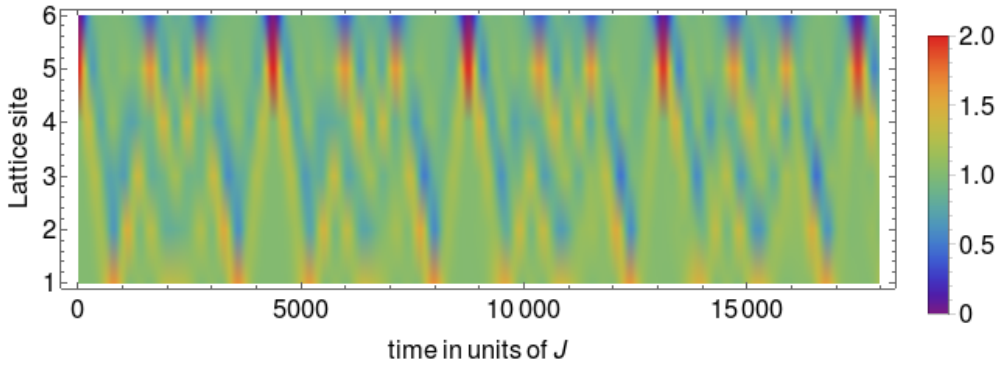

Figure 2.4: Time evolution of the population for the lattice sites of the chain. The color scale goes from blue for zero particles to red for two particles on a given lattice site. The initial state was $|111120\rangle$ and the value of the Stark force in our simulations was $F = 3U + \delta$.

physics from our model? Usually that can be done by a perturbative approach, and it is indeed the direction we will take here. In particular, we will be using the known Schrieffer-Wolff transformation [46, 47]. The explicit calculation of the second order correction using S-W transformation can be found in App. A and the construction of the effective model is done in Sec. 2.2.2.

What about interference? Well, naturally the wave function (WF) of the dipole acquires a phase as it evolves and propagates through the lattice. As it will be justified later, the dipole WF is build up by parts that travel with different velocities and as such they arrive at the edges at different moments in time. Therefore, as the evolution proceed there is an effect of self interference of matter waves that gives rise to the pattern observed in Fig. 2.4.

2.2.2 Effective model

In App. A we found the proper operator that accounts for the hopping of dipoles, it reads

$$O_{\mathrm{SO}} = 2J^2 \left(\frac{1}{F-U} + \frac{1}{F} \right) (\hat{a}^\dagger_{l+2} \hat{a}_{l+1} \hat{a}^\dagger_l \hat{a}_{l+1} + \mathrm{h.c.}) \,, \tag{2.10}$$

where $\hat{a}_l$ ($\hat{a}^\dagger_l$) are bosonic annihilation (creation) operators. Following the form of the Schrieffer-Wolff transformation the effective model (see Eq. (A.5)) reads

$$H_{\mathrm{eff}} = \frac{U}{2} \sum_l \hat{n}_l (\hat{n}_l - 1) + F \sum_l l \hat{n}_l + 2J^2 \left(\frac{1}{F-U} + \frac{1}{F} \right) \sum_l (\hat{a}^\dagger_l \hat{a}^\dagger_{l+2} \hat{a}_{l+1} \hat{a}_{l+1} + \mathrm{h.c.}) \,. \tag{2.11}$$

We have thus an explicit mechanism for the propagation of dipoles and the hopping of single particles is no longer part of the Hamiltonian as a natural consequence of the Schrieffer-Wolff transformation.

One interesting point about the Hamiltonian in Eq. (2.11) is that the center of mass is a conserved quantity (which can be easily proven). That is, $[H_{\mathrm{eff}}, \sum_l l \hat{n}_l] = 0$. Therefore, if we go to the interaction picture in terms of the external Stark field we get

$$H_{\mathrm{I}} = e^{-i\hat{A}t} H_{\mathrm{eff}} e^{i\hat{A}t} - \hat{A} \,, \qquad \text{with} \qquad \hat{A} = F \sum_l l \hat{n}_l \,, \tag{2.12}$$

and thanks to the fact that the center of mass is a conserved quantity, the explicit form of the effective Hamiltonian in the interaction picture reads

$$H_{\mathrm{I}}^{\mathrm{eff}} = \frac{U}{2}\sum_l \hat{n}_l(\hat{n}_l - 1) + 2J^2\left(\frac{1}{F-U} + \frac{1}{F}\right)\sum_l (\hat{a}_l^\dagger \hat{a}_{l+2}^\dagger \hat{a}_{l+1}\hat{a}_{l+1} + \mathrm{h.c.}), \tag{2.13}$$

where this last expression is telling us that seeing from the excitations point of view the lattice is no longer tilted, and actually what the dipoles experience is a transitionally invariant lattice.

2.2.3 From the single-band B-H model to Heisenberg XXZ-model

One of the main goals of this thesis is the study of spin chains by means of Bose-Hubbard like models. To that end we want to take advantage of the effective model accounting for the hopping of dipoles in Eq. (2.11) and connect it to the Heisenberg XXZ-chain.

First, we will work again with the definition of dipole operators that was given in Eq. (2.4). This definition allows us to rewrite the effective Hamiltonian as

$$H_{\mathrm{d}} = (U-F)\sum_l \hat{d}_l^\dagger \hat{d}_l + 4J^2\left(\frac{1}{F-U} + \frac{1}{F}\right)\sum_l (\hat{d}_{l+1}^\dagger \hat{d}_l + \mathrm{h.c.})\,, \tag{2.14}$$

where the term accounting for the contact interaction has disappeared because now we are dealing with excitations and we do not care if such excitations are build up with two or more particles, we only care about the presence or absence of dipoles on a given lattice site. Therefore, the possibilities for the values of occupation number are now zero or one (see Eq. (2.6)). As stated in Sec. 2.2.2 seeing from the dipole point of view, the lattices is not tilted and we arrive to a translational invariant model.

The second step takes advantage of the already constructed mapping from dipoles to spins defined in Eq. (2.7) of Sec. 2.1.2, with the additional fact that such mapping defines the spin ladder operators as

$$\sigma_l^+ = 2d_l, \qquad \text{and} \qquad \sigma_l^- = 2d_l^\dagger\,. \tag{2.15}$$

By going through the mapping onto spin operators we arrive to the Hamiltonian

$$H_s = \frac{W}{4}\sum_l \sigma_{l+1}^z\sigma_l^z + 2J^2\left(\frac{1}{F-U} + \frac{1}{F}\right)\sum_l (\sigma_{l+1}^x\sigma_l^x + \sigma_{l+1}^y\sigma_l^y) - \frac{1}{2}(W-(F-U))\sum_l \sigma_l^z\,, \tag{2.16}$$

which is nothing but the Heisenberg XXZ-chain in presence of an external magnetic field as introduced in Chap. 1, but now all the model parameters are written in terms of the initial Bose-Hubbard parameters. We have the precise identification of the superexchage coupling $\tilde{J} = 2(\frac{2J^2}{F-U} + \frac{2J^2}{F})$, the magnetic field strength $h = \frac{1}{2}(W-(F-U))$, and the anisotropy parameter $\Delta = \frac{W}{4\tilde{J}}$. This identification of the XXZ-chain parameters with the Bose-Hubbard parameters instantly fixes a value to the ratio $\tilde{J}/h$ and Δ. Therefore, we can easily placed our model in the phase diagram of the XXZ-chain (see Fig. 1.3). From the parameters we have used in the simulations we have $\tilde{J}/h \approx \tilde{J}$ since $h \approx 1$, and $\Delta \gg 1$. It implies that our XXZ-chain is deep inside the Néel phase. As a test of this we compute the time evolution of our system starting from a ferromagnet, *i.e*, $|\uparrow\uparrow \ldots \uparrow\rangle$, and find that the system does not evolve. Once we have placed

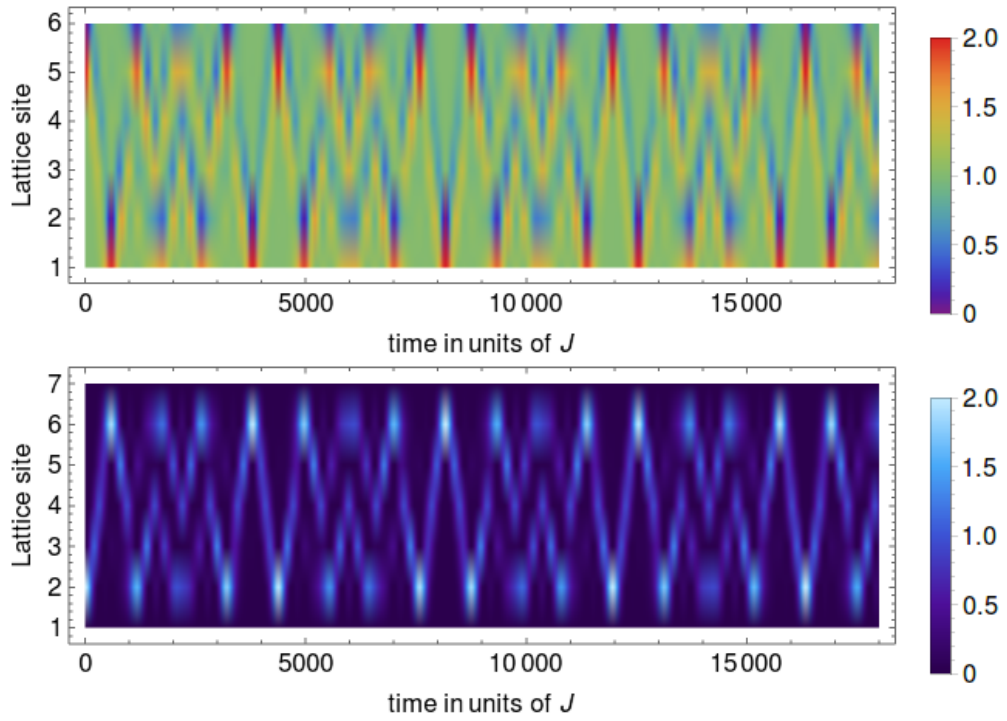

Figure 2.5: Top: Evolution for the population for the different lattice sites in the case of the effective Hamiltonian written in terms of boson creation (annihilation) operators in Eq. (2.11). The initial condition was $|111120\rangle$ and the rest of the parameters as in Fig. 2.4. Bottom: Evolution of the population for each of the different lattice sites with the effective XXZ-model in Eq. (2.16). The initial condition was $|\downarrow\downarrow\downarrow\downarrow\uparrow\downarrow\rangle$, the rest of parameters as in Fig. 2.4. In both cases we re-scale the time scale of the two effective models in order to compare them with the results obtained with the full model, since naturally those time scales do not coincide.

our model in the Néel phase (see Sec. 1.5 and Fig. 1.3) it is easy to see why we have propagation of dipole, by understanding this as propagation of a spin impurity after we have broken the necessary number of bonds starting from an antiferromagnetic ground state.

Now the question is whether or not this effective model, the one in Eq. (2.11) and the one in Eq. (2.16), reproduces the two main characteristics of the time evolution presented in Fig. 2.4. To answer that question we perform the respective time evolution with both effective Hamiltonians, starting with the proper initial condition. The results can be seen in Fig. 2.5, where the time scales of both plots were re-scaled in order to make clearer the comparison between the effective models and the original one.

In the following we will focus on the effective spin model. As we have seen in Sec. 1.5, in any of the two extremal phases (ferromagnetic and Néel) of the XXZ-chain we have possibilities of spin-waves. Our model is in the Néel phase and from the lower panel of Fig. 2.5 we see that indeed the propagation of the impurity occurs. However, as a consequence of the propagation, coherence triggers interference. But interference in the effective case appears later than in the full model. This is because we are moving a single particle and in order to interfere with itself after it bounces back on the edge it needs more time because the accumulation of phase in the wave function as it moves through the lattice takes more time (there is only one object traveling). The

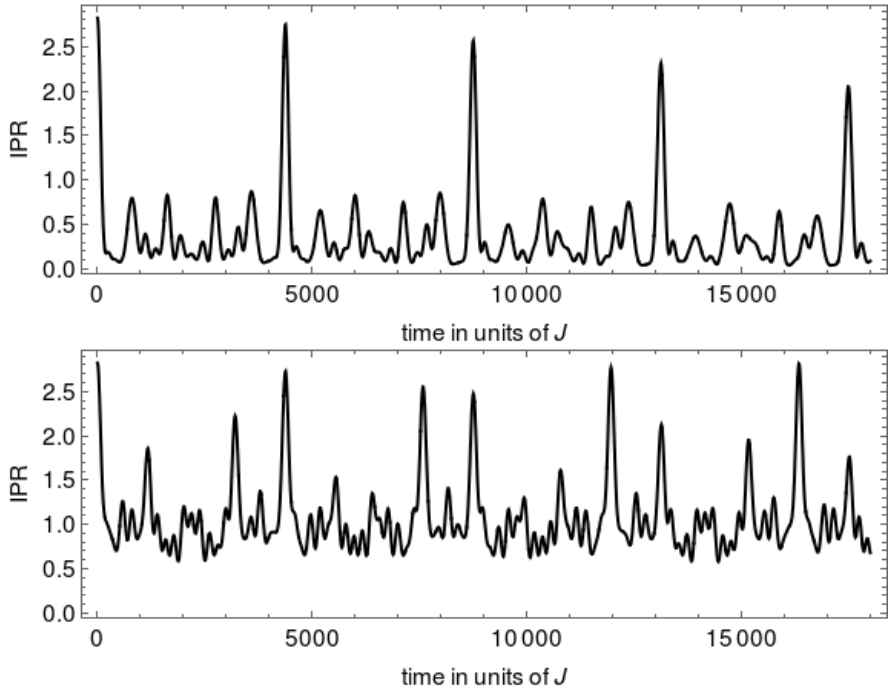

Figure 2.6: Top: IPR for the evolution of the doublon part of the dipole in the case of the Bose-Hubbard model. When contrasted with Fig. 2.4 we see that localization means peaks in the IPR plot and interference means regions of small amplitude. Bottom: IPR for the spin model, the evolution of which was presented in the lower panel of Fig. 2.5. We have re-scaled the time axis in the bottom pannel such that the comparition between the full and effective-spin model is clearer.

same occurs in the case of the effective model written in bosonic operators. Though them act on individual particles, the effect of the operator accounting for the second order process is to move the dipole as a whole. Despite of that, the interference is there, and the pattern has the same structure. Even further it last the same amount of time. This will be studied in detail in the next section.

Among the different observables available to characterize our system, we compute the inverse-participation-ratio-like (IPR) functional. This allow us to have a measure of how localized or delocalized is the occupation distribution in Fig. 2.4 at some moment. This interplay between localization and delocalization is linked with the propagation of the dipole in the following way. When the dipole travels along the lattice it corresponds to a peak of localization and when the interference appears it corresponds to a region of delocalization. The IPR-like functional is defined as

$$IPR_{\mathrm{BH}} = \int_0^L |P_{\mathrm{B-H}}(x;t)|^2 \mathrm{d}x\,, \tag{2.17}$$

$$IPR_{\mathrm{s}} = \int_0^L |P_{\mathrm{s}}(x;t)|^2 \mathrm{d}x\,, \tag{2.18}$$

where P_i with $i = (\mathrm{BH}, \mathrm{s})$ are the probability distributions in the coordinate space that we define

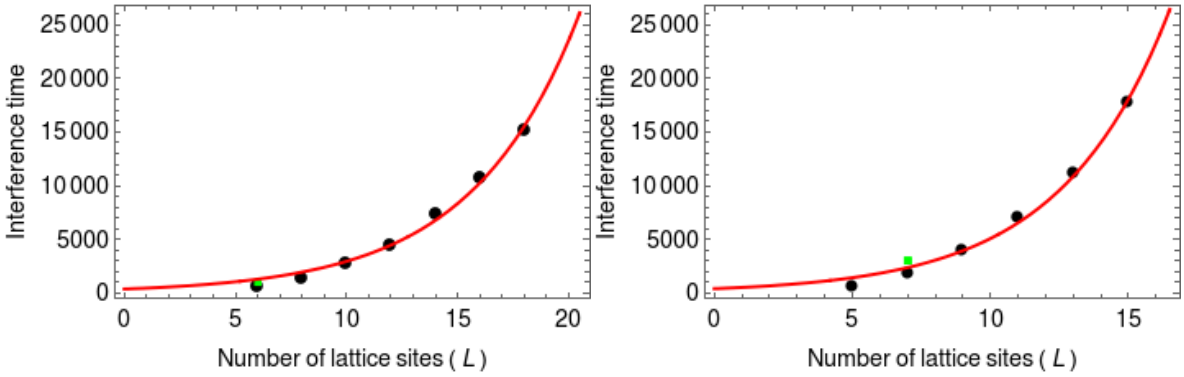

Figure 2.7: Left: Interference time as a function of the lattice length for B-H chains with even number of sites. The exponential fit is a good approximation to the behavior of the interference time as we scale the system size. Right: Time of interference for chains with odd number of lattice sites. Again, the exponential fit suits neatly to the behavior of the interference time as we scale the system. In both cases the cross marker represents the interference time within the full B-H model, for six and seven sites respectively. The green dots are the times within the effective XXZ-chain model and the continuous red line is the best exponential fit for the data.

as

$$P_{\mathrm{BH}}(x;t) = \sum_{l=1}^{L} \frac{1}{2}\hat{n}_l(\hat{n}_l - 1)\delta(x-l) \qquad \text{for bosons}\,, \tag{2.19}$$

$$P_{\mathrm{s}}(x;t) = \sum_{l=1}^{L} \sigma_l^z \delta(x-l) \qquad \text{for spins}\,, \tag{2.20}$$

with n_l the bosonic number operator, and σ_l^z the z-Pauli matrix. It is worth to notice that in the case of the B-H model we only track the localization of the doublon. Since the pair doublon-holon is a whole structure and behaves as it, it is enough to track one of its parts. In Fig. 2.6 we have plotted the IPR for the B-H model and the effective XXZ-chain model, respectively (in Fig. 2.6 the time scale of the bottom pannel was re-scaled to make clearer the comparition). In general, both, the interference phenomena and the interplay between localization and delocalization of the excitation in the successive periods of propagation are preserved. Furthemore, the effective model represents rather well these effects.

2.2.4 Interference in the effective model

The interference phenomena that can be related with the delocalization of the initial excitation along the lattice is without doubt an interesting phenomena. We take advantage of the good mapping of the B-H model into the spin chain to characterize that interference behavior. The reduced basis allows us to estimate the characteristic time of the delocalization, the interference time, faster than using the original model. The results are shown in Fig. 2.7 were we go up to $L = 18$, for which the basis scales linearly with the lattice length. We systematically compute the time evolution of the effective XXZ-chain for lattices the size of which ranged from six sites up to eighteen sites. One major feature that we found when doing this study is that the interference

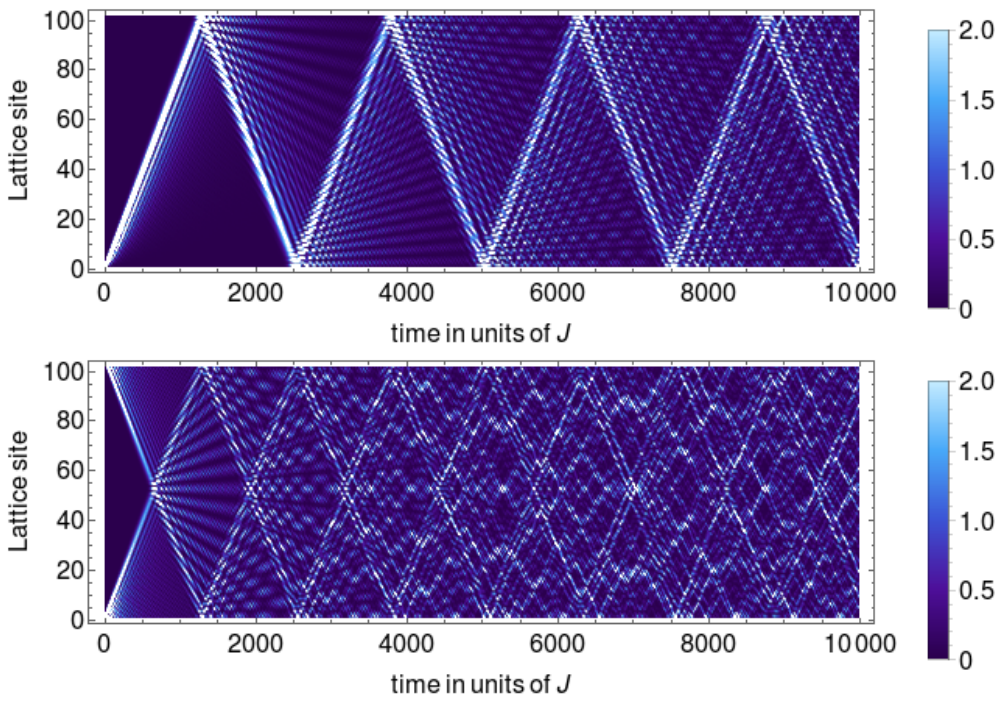

Figure 2.8: Top: Time evolution of the population for each lattice site computed with the effective XXZ-chain spin model for a lattice of $L = 100$ with rigid walls as boundary condition. Emergence of the typical interference pattern of a quantum carpet [45] as a consequence of the scaling of the lattice length. Bottom: Time evolution of the population for each lattice site computed with the effective XXZ-chain model for a lattice with $L = 100$ sites and periodic boundary conditions.

time is sensible to the parity of the number of lattice sites (see App. C). Therefore, lattices with even number of sites were studied apart of those with odd number of sites, the results can be seen in Fig. 2.7. The conclusion of the study is that in both cases, the interference time scales exponentially with the length of the lattice, but the interference time is larger in the case of an odd number of sites.

The reduction to the effective model allowed us to do something else. We are able to investigate the behavior of the interference for large lattices, say, $L = 100$ sites (with L the number of lattice sites). From Fig. 2.7 we can see that for these large lattices the interference time will be really large. However, at this sort of thermodynamic limit the differentiation between even and odd lattice lengths becomes irrelevant. And the system presents a unique long interference pattern. Such pattern can be interpreted as a quantum carpet [45], which is a phenomena known to appear due to the self interference of the wave function when confined in a box. Therefore, this interference-like behavior that appears for small lattices lengths is nothing more that the manifestation of a quantum carpet that emerges when we go to large lattices lengths (see Fig. 2.8). By going to the limit of large systems we find the right explanation we were looking for the interference pattern first depicted in Fig. 2.4. In this limit we can see that the dipole wave function consists of parts that travel with different velocities. Therefore, they arrive at slightly different times at the edge of the lattice and after bouncing back they start to interfere with each other. This phenomena happens always. However, in the case of small number of lattice sites the length of the lattice was not large

enough to make it evident. Additionally and as a mere curiosity we compute the time evolution of the system, for the same initial condition (an impurity in one of the edges), and the same number of sites $L = 100$ but now with periodic boundary conditions. The results can be seen in the lower panel of Fig. 2.8. There we see again the emergence of the quantum carpet as a consequence of the self interference process.

A question that arises is why in the case of periodic boundary conditions (PBC) the self interference appear? This is a natural question, given the fact that with PBC there are no edges in the lattice. The situation of PBC can be interpreted as placing the system in the surface of a cylinder, with time running in the direction of the axes and space wrapping the cylinder. In this scenario it does not matter where we place the single impurity since it sees a translationaly invariant lattice. The WF always splits in parts that travel in both directions. That is, the WF goes around the cylinder clockwise and anticlockwise. Therefore, at some point these two parts are going to met and there the interference appears. So, with PBC we have a different mechanism from that of bouncing back at the rigid walls by which the self interference can happens and hence the quantum carpet emerges.

Before closing this chapter let us give a short summary of what was discussed here. Mainly we deal with the many body problem of the single-band Bose-Hubbard Hamiltonian and how to effectively reduce it to a simple Hamiltonian for dipoles. We have shown that such effective reduction can be linked to spin models, namely, an antiferromagnetic Ising model and the XXZ-chain model. All this when we work with a scheme of energetically locked a Mott state in a tilted lattice and study both the appearance and dynamics of resonant excitations of this Mott state. These excitations are known as dipoles (pairs of doublon-holon in next neighboring sites). We focus our attention in an interference pattern that appears in the strong off-resonant regime of the B-H model. We studied it with the effective XXZ-chain model. We found that such interference pattern appears as a consequence of the self interference of the wave function for the dipole as it travels along the lattice. This is a consequence of the fact that such wave function is made up of components that travel with different velocities (see the different rays that travel along side each other in Fig. 2.8). Each of these components interferes with the others after they bounce back on the rigid edge of the lattice. Finally, we found that in the limit of long lattice lengths this interference has a beautiful interpretation in the emergence of a matter quantum carpet.

Chapter 3

Exploration of the doublon-mediated dynamics in the two-band Bose-Hubbard model

3.1 Motivation

In previous chapters we have worked with the single-band Bose-Hubbard model, and with it we have build quantum simulations of spin chains. That is a great way in which we can take advantage of the characteristic high degree of control featured in the ultracold matter. But it is not the only way. Actually the Bose-Hubbard model exhibits a lot of interesting physical phenomena. Though in many cases the study of it as itself turns out to be quite complex. However, this complexity can be translated to richness in a physical sense [30, 35, 36, 48]. Can we tackle the complexity of a Bose-Hubbard model in such a way that we can control the dynamical transition from one initial to target state(s)? To answer this, there exists different protocols that take advantage, for instance, on the properties of the characteristic quantum spectrum of the system under study [10, 12, 49], the interaction with the environment (an open quantum system), or more precisely techniques for optimal control [50, 51].

Here, aiming to get a clear answer to that question we propose a toy model based on a two-band Bose-Hubbard Hamiltonian where the only transport mechanism is a doublon-mediated inter-band coupling. We explore the manifold of accessible states. This exploration was done in two different ways. First, we shake in time the optical lattice with an external pulse (see Sec. 3.3). Second, we look for the existence of resonances allowed by the doublon-mediated inter-band coupling and we perform one-way parametric evolutions around the respective first order resonance (see Sec. 3.4).

3.2 Theoretical model

In Sec. 1.4 we discussed the explicit form of the Bose-Hubbard model. There, we stated that one can truncate the sum over the band index in order to have an approximation to the whole system.

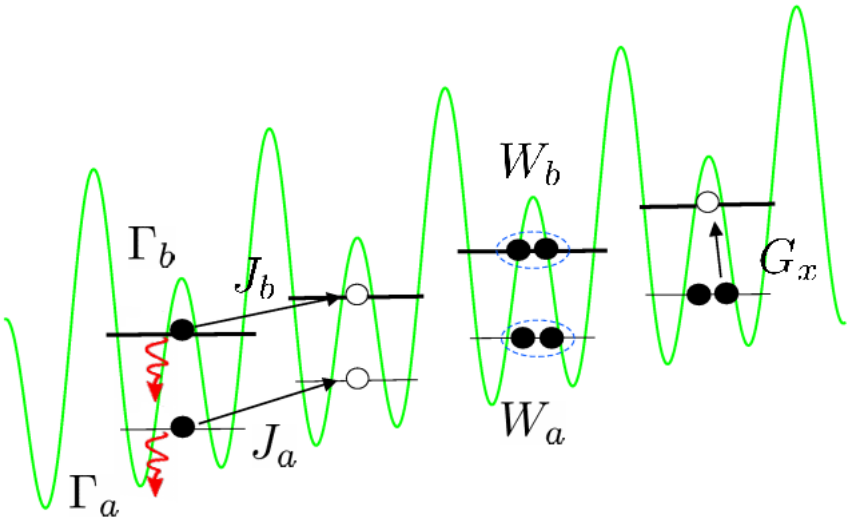

Figure 3.1: Schematic representation of the different processes that take place under the two-band Bose-Hubbard Hamiltonian in Eq. (3.1) with the doublon-mediated inter-band coupling.

One way to obtain the two-band Bose-Hubbard model is by truncating that sum up to $\alpha = 2$ in Eqs. (1.16)–(1.18) (see [36, 52]). Here, we have interest in a different two-band Bose-Hubbard model. The Hamiltonian that we work with through this chapter is

$$H = \sum_l \sum_{\beta=a,b} \left[-\frac{J_\beta}{2}(\beta_{l+1}^\dagger \beta_l + \text{h.c.}) + \frac{W_\beta}{2} n_l^\beta (n_l^\beta - 1) + 2\pi F l n_l^\beta - i\Gamma_\beta n_l^\beta \right] + \sum_l \Delta_g n_l^b + \sum_l G_x (b_l^\dagger a_l n_l^a (n_l^b - 1) + n_l^a (n_l^a - 1) a_l^\dagger b_l) \,, \quad (3.1)$$

which is a model including the first two energy Bloch bands. The system is effectively open by introducing the respective decay rates ($\Gamma_{a,b}$) of each band [49]. A schematic representation of the process we consider in the Hamiltonian in Eq. (3.1) can be seen in Fig. 3.1. The interband coupling is realized via a term mediated by G_x that makes the interband transport possible only when there are doublons, *i.e.*, two particles in the same lattice site, in the lower band. This term can be introduced as a second order correction to the main Hamiltonian presented in [52]. This correction can be achieved using a Schrieffer-Wolff like transformation [47] (see App. A).

3.3 Shaking the lattice

It is known that driven systems offer a whole and rich new physics as is proven for example by the existence of the Floquet topological insulators and the appearance of magnetic like behavior in neutral atoms systems [9]. Here, instead of looking for new physics we want to do a dynamical exploration. That is, we look for dynamical stable states (or structures) which are robust against the coupling to an environment (a bosonic reservoir).

Table 3.1: Bose-Hubbard parameters.

V_0	S_0	Δ_g	J_a	J_b	W_a	W_b	G_x
11	3	0.108	0.006	0.006	0.034	0.034	0.03

Table 3.2: Fock basis for the 2/2 system.

i	1	2	3	4	5	6	7	8	9	10
state	$\|11;00\rangle$	$\|10;10\rangle$	$\|10;01\rangle$	$\|01;10\rangle$	$\|01;01\rangle$	$\|20;00\rangle$	$\|02;00\rangle$	$\|00;20\rangle$	$\|00;02\rangle$	$\|00;11\rangle$

To take advantage of the new term including inter-band transport via doublons we tilt the lattice, such that the doublon triggers interband transport. That is, the force at which the doublon can be destroyed to take at least one particle from the lower band to the upper band. This is done by the external force defined as

$$F = F_0 + F_A \sin^2(\omega_q t)\,, \tag{3.2}$$

where $F_0 = \frac{W_a}{2\pi}$ is the value of the external force bringing close in energy a single-particle level with a two-particle level in the next neighboring site (towards the direction of the tilt), $F_A = \frac{\Delta_g - W_a}{2\pi}$ is the amplitude of the oscillation, and $\omega_q = \frac{\Delta_g - 2W_a}{2\pi}$ is the oscillation frequency. We may notice that the oscillation happens between the two-particle energy level and the single-particle first order resonance.

3.3.1 Results

We work with the smallest possible non trivial system, say two particles in two wells (2/2), where the filling factor is defined as N/L with N the number of particles and L the number of sites. The results presented in this section are obtained for that system and we expect to see a similar behavior when we move on to the larger system (4/4). Additionally, we have worked with the set of Bose-Hubbard parameters as specified in Table 3.1 in a way that we can guarantee $J_{a,b} \ll W_{a,b}$, with $\Gamma_{a,b}$ at least one order of magnitude smaller than $J_{a,b}$. These parameters were taken from App. 1 in [35]. For the numerical simulations we study the population inversion as our main observable, that is the difference between the population $M_b(t)$ of the upper band and the population $M_a(t)$ of the lower band,

$$M_b(t) - M_a(t) = \frac{1}{N}\left[\langle\psi(t)|\sum_l \hat{n}_l^b|\psi(t)\rangle - \langle\psi(t)|\sum_l \hat{n}_l^a|\psi(t)\rangle\right]. \tag{3.3}$$

We compute the time evolution looking for a stationary state. First, we study the main probability of appearance for each of the states in the Fock basis (the Fock basis was ordered as in Table 3.2) with the ratio Γ_b/Γ_a. The results are shown in Fig. 3.2. The value $\Gamma_b/\Gamma_a = 1$ splits the dynamics into two regimes. For $\Gamma_b/\Gamma_a > 1$ the probability remains in the initial state $|11;00\rangle$, while for $\Gamma_b/\Gamma_a < 1$ there is a non-trivial evolution, for instance, in the case of $\Gamma_b/\Gamma_a \ll 1$ the

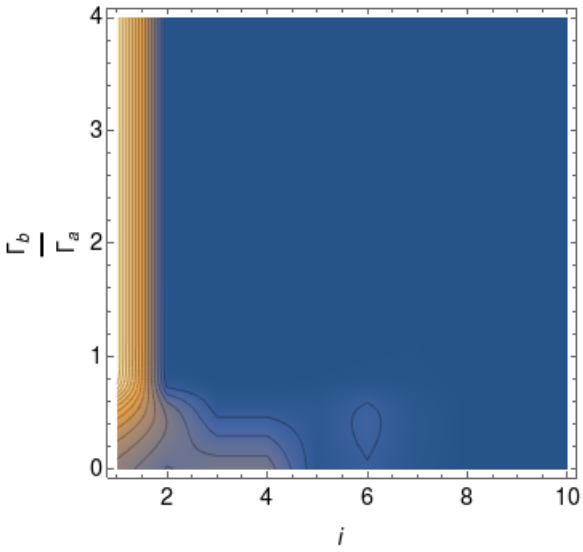

Figure 3.2: Average probability for each of the states in the Fock basis as a function of the ratio between the decay rates for all elements of the basis. We see that after a value $\Gamma_b/\Gamma_a = 1$ only the state $|11;00\rangle$ is excited by the external force. The region of interest for us is $\Gamma_b/\Gamma_a \ll 1$.

states 3 and 4 get excited. We focus on the latter region. Although this division is valid only in the time scales and values of parameters at which we have worked here, it can be shown that for longer time scales there is a non trivial evolution for $\Gamma_b/\Gamma_a > 1$. Here, we are not interested in such long time scales.

With the ratio Γ_b/Γ_a fixed to the proper value, we turn off the modulation and compute the time evolution of our system. The results can be seen in Fig. 3.3, where it is evident that we reach a final state which is non stationary. It is a superposition of four states, and two of them are $|10;01\rangle$ and $|01;10\rangle$, the superposition of which is of interest due to the fact that it resembles a Bell's state $|10;01\rangle \pm |01;10\rangle$. But there is an undesirable contribution of other two states.

As a final test we turn on the shaking and performed the same computation as before, we look at the population inversion and the final state after the evolution. There is a stationary state and is given by the wanted superposition. From Fig. 3.4 is clear that the shaking cleans the final state giving us only the two desired states and in an equally weighted superposition. Hence we can conclude that in the $2/2$ system our scheme is successful.

Now we ask what would happen when we go to a larger system, do the superposition we just found survives? One can think that such superposition have to appear somewhere in the time evolution. To check that we work with a $4/4$ system. The first thing we need to guarantee is that the population inversion effectively approaches zero at some point in time and remains like that. That is, we end up with an equal number of particles in the lower an upper band. To check that we have computed the mean population inversion as a function of the ratio Γ_b/Γ_a, the results can be viewed in the right panel of Fig. 3.5.

As we can see the average population inversion as a function of Γ_b/Γ_a saturates at the value -1 for outside the region $\Gamma_b/\Gamma_a < 1$. That is, outside that region there is a small probability of finding a final state with equal occupation of both bands. However, inside $\Gamma_b/\Gamma_a < 1$ the population

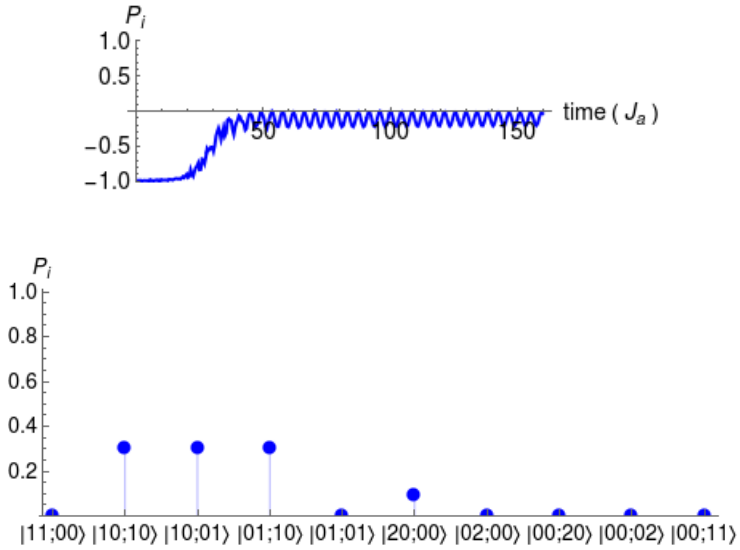

Figure 3.3: Top: population inversion as a function of time for the system without shaking. We see that even when the population inversion goes toward zero there is no stationary state. Bottom: final state found at the moment we stop the time evolution. From the behavior of the population inversion we see that there are oscillations between the states being excited (states 2, 3, 4, and 6 of Table 3.2).

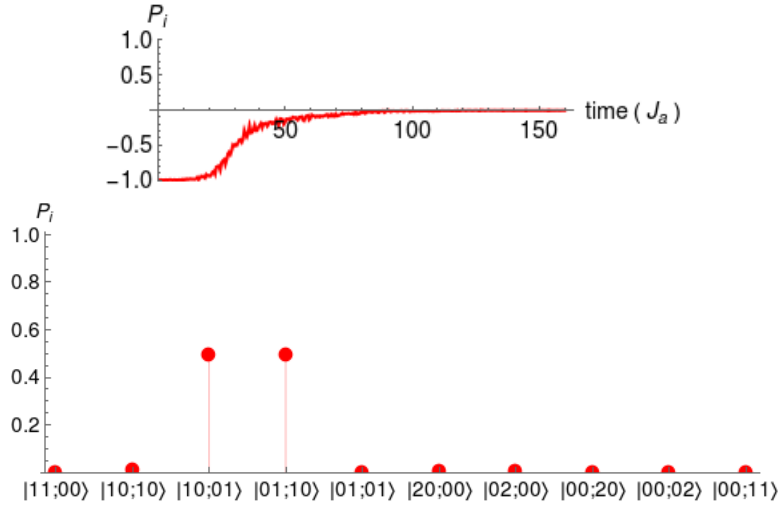

Figure 3.4: Top: population inversion as a function of time for the system with shaking. Now there is a saturation of the population inversion at zero, hence we have an stationary state. Bottom: final and stationary state found at the moment we stop the time evolution. This state is given by an equally weighted superposition between $|10;01\rangle$ and $|01;10\rangle$.

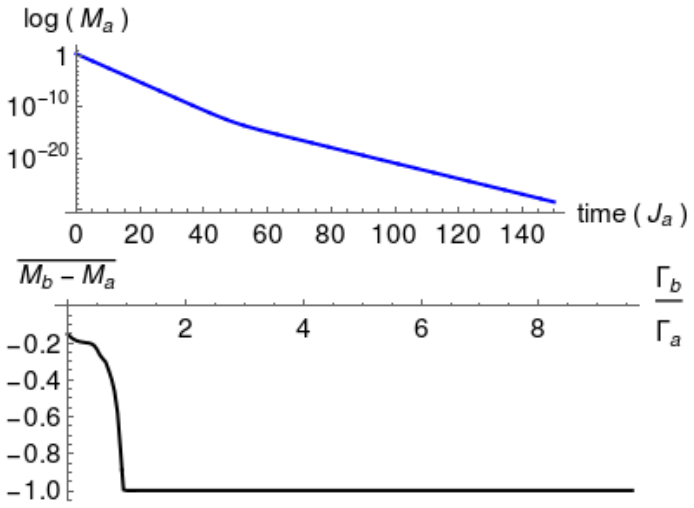

Figure 3.5: Top: behavior of the population in the lower band as a function of time without performing the renormalization after each evolution step. As expected from a dissipative dynamics, the population decays exponentially. Bottom: mean population inversion as a function of the ratio Γ_b/Γ_a for the $4/4$ system. We can see that even in the region $\Gamma_b/\Gamma_a < 1$ that was the region of interest in the case of the $2/2$ system, the population inversion never approaches zero. Therefore, the final state is not a state with equal number of particles in each band.

inversion remains smaller than one, which means that it is possible to have a final state with equal occupation of both bands. The population inversion never goes to zero due to fact that we are averaging it and there is always a contribution of some states with a varied occupation of both bands as we evolve towards the final state. However, in our numerical test we have not found the wanted superposition, though we find final states with equal occupation of the bands. We thus conclude that the shaking scheme works only in the case of the minimal system, but fails when we increase the number of lattice sites.

Comments regarding the dissipative dynamics.

One important clarification we shall do is about the dissipative dynamics we are implementing here. When we open the system we do not just add a decay rate to each band which makes those states metastable, we are allowing particles to scape from our system.

Thus every now and then we have to renormalize the probabilities of our evolution vector, in particular after each evolution step we performed the renormalization. Thanks to the fact that the evolution steps we had taken were always from zero to the respective time value at which we are evolving we did not alter the final result.

However, just to verify the correct behavior of the dissipative dynamics in our system we did a calculation of the population in the lower band as a function of time without performing the renormalization after each step. The results can be seen in the left panel of Fig. 3.5, and as expected from this kind of dynamics the population decays exponentially in time due to the escaping of particles.

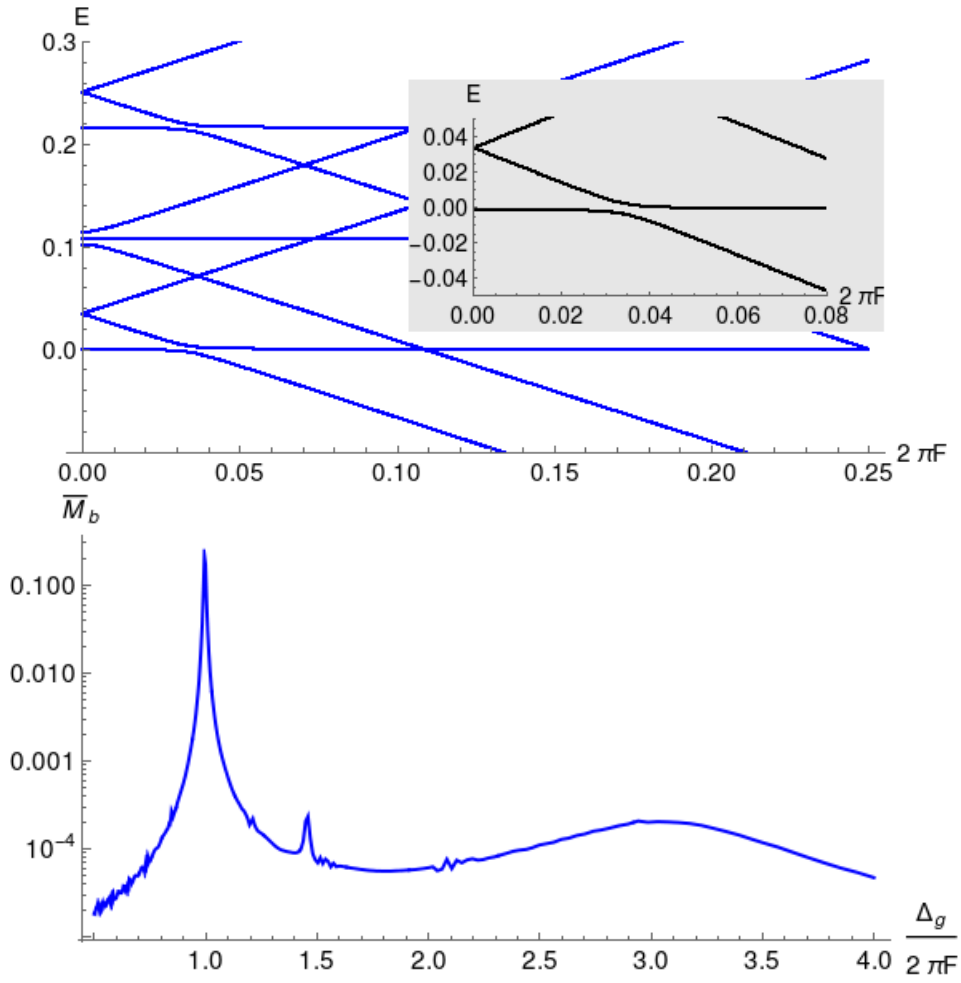

Figure 3.6: Top: energy spectrum of the Hamiltonian in Eq. (3.1) for the minimal system as a function of the force amplitude F. It is characterized by the presence of AC (see inset). Bottom: long time average occupation of the upper band as a function of the Stark force. We can see the resonant behavior in three points (with $\Delta_g = 0.108$).

3.4 Parametric evolution

As in the previous section we have strong interest to investigate what is the resulting dynamics of the Hamiltonian introduced in Eq. (3.1) when we vary the external Stark force. We have already presented the results in the minimal model and the expected results with the scaling of the system for a sinusoidal-like modulated Stark force. Here, we want to use a different approach, namely parametric evolution. By parametric evolution we mean a time evolution controlled by a single parameter which dictates the speed at which the evolution happens. In particular we have interest to implement such evolution to carry our initial state across an avoided crossing (AC). We understand AC as the phenomenon of repulsion between energy levels as a function of a control parameter.

The transit across the AC can be done by setting the external Stark force as a time dependent

parameter $F(t)$ and choosing the parameter governing the evolution as the sweeping rate α (see Eq. (3.4)). The goal of the present section is to look for such couplings between energy levels from different bands. Once we have found them, manifested as an AC, we evolve the initial Mott-like state parametrically across the AC looking for the different final states and finally comparing with the states that were found with the modulated external Stark force in Sec. 3.3. The present development was done mainly following Parra-Murillo (see Chap. 4 of [35]), specially the study of the different sweeping rates.

3.4.1 Methods and results

Since the AC is a manifestation of the coupling between two energy levels it is natural to link them with resonances. By resonance we understand the situation in which the external field is such that it brings to a degeneracy of the single-particle levels from different bands (see Fig. 2.1).

The first test we have to do is to check for the existence of resonances under the influence of the doublon-mediated inter-band coupling. Here we initially worked with the minimal model, say two wells with two particles (2/2), and rigid walls or open boundary conditions. We compute the energy spectrum of such system and the long time average occupation of the upper band as a function of the Stark force for the initial Fock state $|11;00\rangle$ (similarly we compute such signal for other initial states, see App. B). Both results can be seen in Fig. 3.6.

In particular we observe the presence of AC in the energy spectrum and the respective resonant behavior at the same positions. We will focus our study around the region $\Delta_g/2\pi F \approx 1$ where we find the highest resonant response. Now we need to define the proper form of the external force to perform the navigation. Following Parra-Murillo (see chapter 4 of [35]) we will perform up to one sweep. We define the Stark force by

$$F = \alpha t + F_0\,, \qquad \text{and} \qquad t_\alpha = \frac{F_f - F_0}{\alpha}\,, \tag{3.4}$$

where F_0 and F_f are the initial and final values of the force such that we navigate the region around the first order resonance, which is the one we have interest in, and t_α determines the total time for the evolution. We shall notice that different values of α will provide different time steps. Therefore, α is a control parameter for the kind of dynamics we are implementing. The dynamics can be enclosed in three different regimes: adiabatic, diabatic (or sudden), and non-adiabatic [53]. In the following we have interest in the adiabatic regime with $\alpha/\delta(F_f - F_0) \ll 1$. By adiabatic we mean an evolution in which the system remains in an eigenvalue of the instantaneous Hamiltonian. In this regime, as we show later, we find a major appearance of different states as final ones without contribution of the initial state.

Now we only need to find the proper value of α and get the desired adiabatic evolution. In order to do that we build a mesh of α values and compute the time evolution of an initial state $|11;00\rangle$ and check for the states participating in the dynamics for different α values. We present the results of that study in Fig. 3.7. We can recognize there three different regimes, each one associated with a different kind of dynamics. Although there is an ambiguity when we want to define the boundaries of each regime, we have found that for our study, the adiabatic regime ranges between $(0,\ 0.1)$, the non-adiabatic regime between $(0.1,\ 0.2)$, and the diabatic regime between $(0.2,\ 1)$ in units of $\frac{\alpha}{\delta(F_f - F_0)}$.

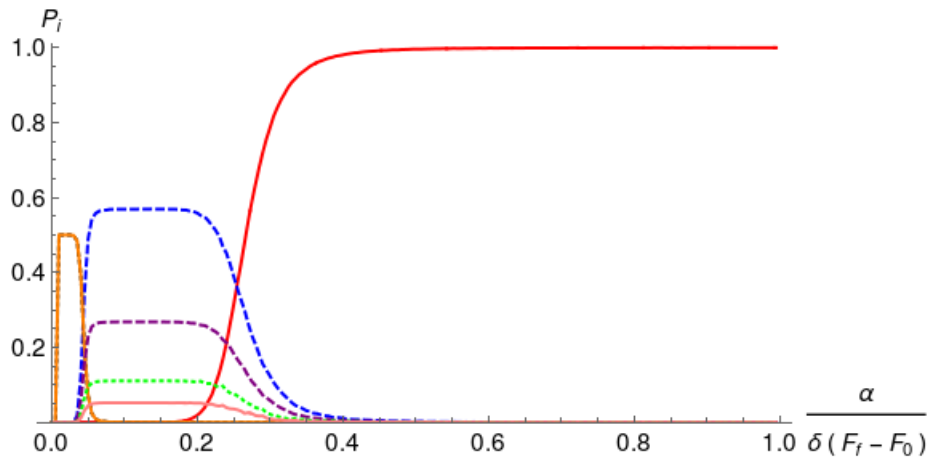

Figure 3.7: Probability of participation (P_i) for the states that take part in the dynamics as function of the sweeping rate α. We can clearly observe the three different regimes of dynamics governed each one by a different set of α values. We have, for small $\alpha \to |10;01\rangle$ (black) and $|01;10\rangle$ (orange) in an equally weighted superposition, for intermediate $\alpha \to |10;10\rangle$ (blue), $|01;01\rangle$ (purple), $|20;00\rangle$ (green), and $|02;00\rangle$ (pink), for large $\alpha \to |11;00\rangle$ the initial state in red. Here, α represents the sweeping rate, F_f and F_0 are the final and initial values of the Stark force between which the evolution takes place, and δ is a characteristic parameter that measures the width of the AC.

For small α values we lost the information of the initial state and gain some new and interesting states as consequence of the adiabatic evolution. For example, an equally weighted superposition between the two alternating states, given by $\frac{1}{\sqrt{2}}(|10;01\rangle + |01;10\rangle)$, where the color code is $|10;01\rangle$ in black and $|01;10\rangle$ in orange. On the other hand, for intermediate values of α we find a four-state superposition given by $|10;10\rangle$ (blue), $|01;01\rangle$ (purple), $|20;00\rangle$ (green), and $|02;00\rangle$ (pink). As a consequence of the non-adiabatic dynamics the navigation process is not complete and we end up with an intermediate state as our final state. Finally, for large α values we find the diabatic regime, where we navigate the spectrum fast enough and the system is not able to couple to other states ending up in the same initial state $|11;00\rangle$ in red.

From the results presented in Fig. 3.7 we will focus our attention in the first region, the adiabatic region, since it is there where we find a successful navigation process. From our numerical computation we were able to obtain a given α within that region and perform the time evolution of our system. The results can be seen in Fig. 3.8. At this point we should notice that, besides the exploration of the doublon induced dynamics, we have found that such dynamics can sustain an interesting superposition as the one of Sec. 3.3 which resembles an entangled Bell-like state for the minimal system in the model defined by the Hamiltonian introduced in Eq. (3.1).

Before closing this section we will deliver some comments regarding the dynamics of a larger system $(4/4)$, and once there, we should check if it is possible to find some interesting superpositions as the one we just found for the minimal $(2/2)$ system. For the $4/4$ system we followed a similar procedure than that of the $2/2$ system. First we check if in the energy spectrum there were regions with AC at which we can perform spectral navigation. To that inquiry we found an affirmative response (results can be seen in App. B). Then we compute the time evolution of a given initial state $|1111;0000\rangle$ for each of the α values in the proper mesh. In Fig. 3.9 we present the above mentioned results.

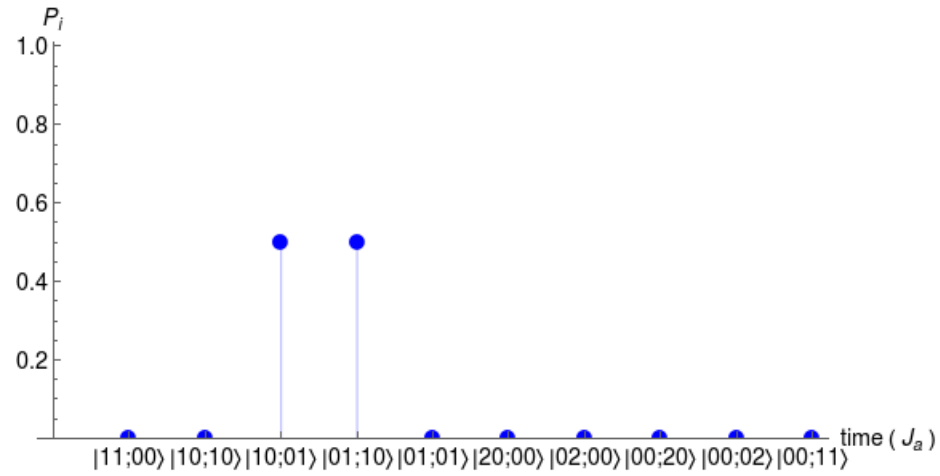

Figure 3.8: Final state after the evolution for a value of α with the region of adiabatic dynamics. The state is given by an equally weighted superposition between $|10;01\rangle$ and $|01;10\rangle$. The value of α that we used in the calculation was $\alpha = 1.33 \times 10^{-6}$.

Table 3.3: Dynamical states for the initial condition $|1111;0000\rangle$. We tabulate the maximum probability P_i (on the left of each column) of finding the i-th state (on the right of each column) in the final state.

Diabatic region		Non-adiabatic region		Adiabatic region	
$P_{21} = 0.9994$	$\|1111;0000\rangle$	$P_{49} = 0.1252$	$\|1011;1000\rangle$	$P_{242} = 0.7638$	$\|1000;0210\rangle$
		$P_{67} = 0.1254$	$\|1101;0100\rangle$	$P_{251} = 0.2224$	$\|0001;0120\rangle$
		$P_{81} = 0.1251$	$\|1110;0010\rangle$		
		$P_{149} = 0.2754$	$\|1010;1010\rangle$		
		$P_{160} = 0.1298$	$\|0110;0110\rangle$		
		$P_{229} = 0.1300$	$\|0100;0300\rangle$		
		$P_{236} = 0.2683$	$\|1000;1110\rangle$		
		$P_{240} = 0.1804$	$\|0010;0210\rangle$		
		$P_{249} = 0.2350$	$\|0100;0120\rangle$		

From Fig. 3.9 we can see that the diabatic region is governed by the initial state, meaning that we go through the AC too fast and the system does not have time to coupled to another state. In addition, the non-adiabatic region has a high population of different states. Finally, the adiabatic region, the one at which we have found a successful navigation process, is mainly governed by two states, $|1000;0210\rangle$ and $|0001;0120\rangle$, with a higher contribution of the first one.

In Table 3.3 we find the respective states, with their respective maximum participation probability labeled by their position in the Fock basis, for each one of the three dynamical regions, with the proper color code to make the association easier. We may notice that the states sharing the same color label appear as an equally weighted superposition.

In general terms the global results are not too far from those obtained in the $2/2$ system. However, we were not able to find an equally weighted superposition of alternating states. In fact the adiabatic region favors the appearance of states with a population of three particles in the upper

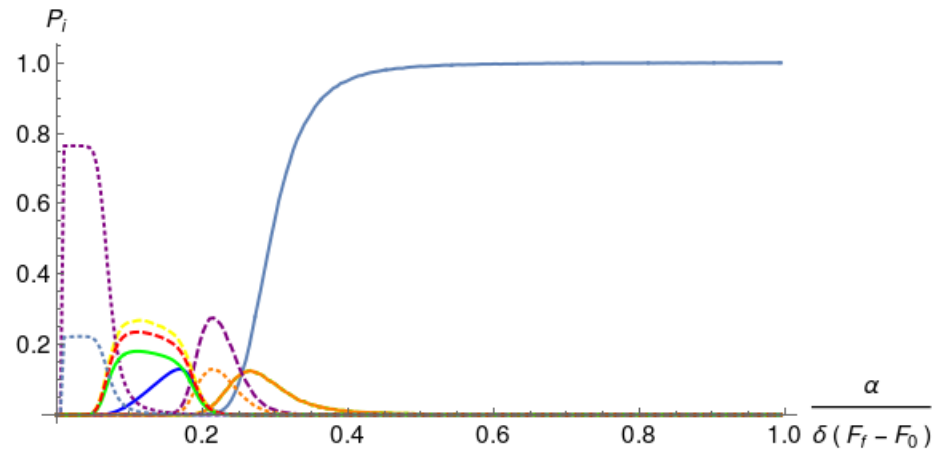

Figure 3.9: Different states participating in the navigation process for the initial state $|1111;0000\rangle$. There are three different dynamical regions, adiabatic, non-adiabatic and adiabatic, just as in the case of the 2/2 system. However, the interplay between the states starts to be more complex due to the large number of states involved on the evolution.

band. We do find some states with equal population of both bands, but they were not alternating states and were inside the non-adiabatic regime of α values, as for example $|0110;0110\rangle$.

We performed the same calculation for other two initial conditions, say $|0202;0000\rangle$ and $|2020;0000\rangle$, since they are easily accessible states from the state $|1111;0000\rangle$ through the first order resonance between a single-particle level and a two-particle level, both states in the first band (see [39, 40]). These results can be seen in App. B. Also, when we take a look at the coupling obtained in Eq. (A.15) of App. A we see that the Schrieffer-Wolff transformation introduces an inter-site coupling rather than a intra-site coupling as the one consider for the calculations of this section. Due to that we repeated the same set of calculations for a Hamiltonian with such a coupling (see further details in App. B).

Last but not least, let us give a brief summary. We have devote this chapter to the study of the dynamical consequences of the inclusion of a doublon-mediated interband coupling to the two-band Bose-Hubbard model. The time evolution was done in two different ways. First, by shaking the lattice, and second by searching for the presence of AC in the energy spectrum and performing parametric evolution in order to go through them. For both cases the external Stark force was a time-dependent parameter $F(t)$ over which we have control. The study had two stages. The first one was developed on the minimal system, *i.e.*, two particles in two wells (2/2). The second one refered to the investigation of the robustness of the final states against the scaling of the lattice length. The main conclusion is that, the doublon-mediated interband coupling allows us to target some interesting states but such states are not robust against the scaling of the system. Finally, a broader set of results can be found in App. B.

Chapter 4

Conclusion and outlook

Throughout this thesis we did two things. First, we use a well defined quantum simulator based on a Heissenberg chain to characterize second order processes in the single-band Bose-Hubbard model far from the known single and many-body resonances. This simulation was based on a previously explored simulation of the antiferromagnetic Ising chain [7]. The quantum simulation of this chain takes advantage of the fact that once we energetically lock the Mott insulator state on a tilted lattice, a strong tilt couples the Mott state to a certain manifold by resonant transitions. These transitions are given by movement of particles between next neighboring sites when the energy level of a single particle and two particles are degenerated. Finally, we can define pseudo-spins based on this transitions to make the link between the two models. Later we found the existence of second order processes that are not explicitly considered within the single-band B-H model. These processes consist on the propagation of the holon-doublon quasiparticle along the lattice. We compute the explicit form of the proper operator accounting for this process using a Schrieffer-Wolff transformation. The link between the B-H model and the Heissenberg XXZ-model is obtained by the same pseudo-spin mapping as in the simulation of the antiferromagnetic Ising chain. With this identification we found that the propagation of the holon-doublon quasiparticle can be interpreted as a spin-wave in the XXZ-chain.

Second, we present a variation of the open two-band B-H model that couples the bands by means of a doublon-mediated inter-band coupling. These coupling has its justification in the fact that when the Stark field induced resonant enhance tunneling in the first band, the leading process is the creation of doublons in that band. We explored the dynamics of the system finding a complete set of the allowed states. First, for the minimal system the main result was that among the accessible states there is one that resembles a Bell state. Later, when exploring the dynamics of larger systems we did not find such a state, from which we conclude that such a state is not robust against the scaling of the system, at least no under the two approaches of the dynamics studied in this thesis.

There are open questions in both cases. In the quantum simulation we dealt with, it is necessary a deeper study of the second order processes in the single-band B-H model in order to propose an experimental scheme that could look for them and to get a better understanding of their interpretation as spin waves. In the case of quantum control presented in Chap. 3, it is necessary to do additional studies of the consequences of the doublon-mediated inter-band coupling and the proper mechanism by means of which it appears in the two-band B-H Hamiltonian.

Additionally, there is a need of finding the right protocol that allows us to have a better control over the dissipation such that the obtained Bell-like state in the minimal system survives the scaling of the system.

Appendix A

On the Schrieffer-Wolff transformation

Unitary transformations are among the more useful resources theoretical physics count with to build a better interpretation of some initially tricky problem. The possibility of re-writing a problem in a more friendly and handy way has shown to be of great advantage. Sometimes they unveil deep connections between physical systems that one initially could have thought as totally uncorrelated. For instance, this is the case of the Ising model in a transverse field and the one dimensional p-wave superconductor connected through the Jordan-Wigner transformation (see Chap. 5 of [54]), or the connection between the single-impurity Anderson model and the Kondo model proved in 1966 by Schrieffer and Wolff [46] using the unitary transformation named after them. The latter transformation constitutes the topic of this brief appendix. For some rigorous review of the Schrieffer-Wolff transformation (SWT) we recommend [55].

A.1 General remarks

The SWT is an unitary transformation that allows us to effectively isolate low energy physical phenomena of a system under study. In this sense, it provides us with an effective representation of our problem that in many examples has been proven to be in excellent agreement with the physics and information we get from the full system [46, 56, 57].

There are scenarios in which some physical systems manifest second or higher order processes that occur as consequence of first order processes like hopping or tunneling being virtual ones. One can think of a one dimensional lattice system described by a Hamiltonian that allows hopping of particles only between next neighboring sites. This system might, nevertheless, exhibit a regime which features long range hoppings. Such processes can be understood as composed by next neighboring hoppings that virtually occur as intermediate steps. In this situation one's interest is to write a Hamiltonian which accounts for those second order hoppings. The SWT accomplishes precisely this: it allows one to get rid of the parts of the Hamiltonian that account for the first order process and introduces the proper operator for the second order process (and higher orders if necessary) which is built as products of first order process operators.

As a starting point let us think of a Hamiltonian that can be written as

$$H = H_0 + V \,, \tag{A.1}$$

where H_0 is a Hamiltonian for which the eigenvalues are known and V stands for a perturbative term. The first step consists in a canonical transformation of the form

$$H_{\text{eff}} = e^S H e^{-S}\,, \tag{A.2}$$

where the operator S is called the generator and it has to be found in a way that no linear terms appear in the Hamiltonian H_{eff}. Using the Baker-Campbell-Hausdorff formula, the transformed Hamiltonian can be written as the expansion

$$H_{\text{eff}} = \sum_{m=0}^{\infty} \frac{1}{m}[S,H]_m = H + [S,H] + \frac{1}{2}[S,[S,H]] + \frac{1}{6}[S,[S,[S,H]]] + \dots\,. \tag{A.3}$$

By imposing that $V = -[S,H_0]$ we can achieve the required Hamiltonian without the linear terms. Including the expression for V in the series expansion in Eq. (A.3) in an iterative way, one gets

$$H_{\text{eff}} = H_0 + \frac{1}{2}[S,V] + \frac{1}{3}[S,[S,V]] + \frac{1}{8}[S,[S,[S,V]]] + \dots\,, \tag{A.4}$$

where we have already included higher order terms. Since we are interested only in the description of second order processes, we may truncated the expansion up to that order. It will thus look like

$$H_{\text{eff}} = H_0 + \frac{1}{2}[S,V]\,. \tag{A.5}$$

At this point it remains to introduce the Hamiltonian of the specific problem we are studying and compute the respective generator. However, this is in general not an easy task. It is easier to compute the specific matrix elements, that is, we use the eigenstates of H_0 to write

$$\langle i|H_{\text{eff}}|j\rangle = \epsilon_{i,j}\delta_{i,j} + \frac{1}{2}\left(\langle i|SV|j\rangle - \langle i|VS|j\rangle\right)\,. \tag{A.6}$$

The matrix elements of SV and VS can be further evaluated by introducing the identity sum $\sum_k |k\rangle\langle k| = 1$. Eq. (A.6) can be thus written as

$$\langle i|H_{\text{eff}}|j\rangle = \epsilon_{i,j}\delta_{i,j} + \frac{1}{2}\sum_k \left(\langle i|S|k\rangle\langle k|V|j\rangle - \langle i|V|k\rangle\langle k|S|j\rangle\right)\,. \tag{A.7}$$

Using $V = -[S,H_0]$ it follows

$$\langle i|V|j\rangle = -\left(\langle i|SH_0|j\rangle - \langle i|H_0S|j\rangle\right) = (\epsilon_j - \epsilon_i)\langle i|S|j\rangle\,, \tag{A.8}$$

where we have exploited the fact of $|i\rangle$ and $|j\rangle$ being eigenstates of H_0. Eq. (A.8) implies

$$\langle i|S|j\rangle = \frac{\langle i|V|j\rangle}{\epsilon_i - \epsilon_j}\,. \tag{A.9}$$

Plugging this into Eq. (A.7) we find

$$[H_{\text{eff}}]_{i,j} = \epsilon_{i,j}\delta_{i,j} + \frac{1}{2}\sum_k \left(\frac{1}{\epsilon_i - \epsilon_k} - \frac{1}{\epsilon_k - \epsilon_j}\right)\langle i|V|k\rangle\langle k|V|j\rangle\,, \tag{A.10}$$

where the complete set of states $|k\rangle$ that we introduced in Eq. (A.7) turns out to be all intermediate or virtual states that allows for the transition from state $|i\rangle$ to state $|j\rangle$. The identification of these intermediate states is an easier task that the full calculation of the generator S. In the next sections we apply the Schrieffer-Wolff transformation as presented here to the Bose-Hubbard Hamiltonians we study in Chaps. 2 and 3.

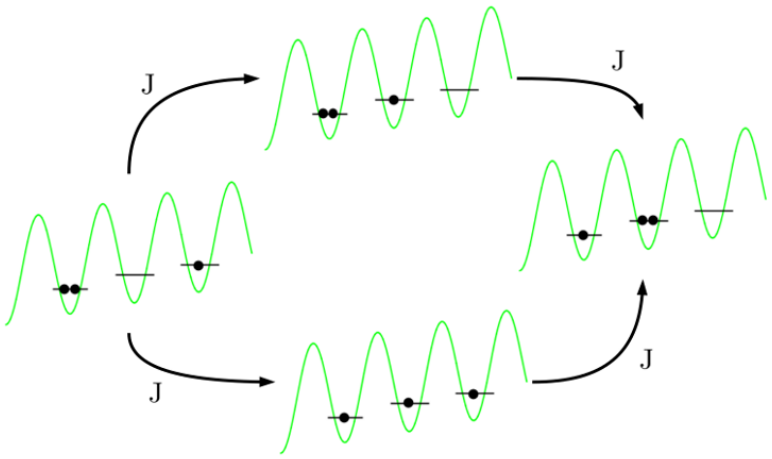

Figure A.1: Schematic representation of the second order processes corresponding to the hopping of a dipole between successive sites. This time the intermediate states corresponds to the dipole vacuum (Mott state), and a sate where the initial dipole has been separated and its individual constitutents are in different sites separated by at least one well.

A.1.1 Application of the SWT to the single-band Bose-Hubbard model

We are interested in second order processes in the single-band Bose-Hubbard model. These processes can be represented as successive hoppings of particles, as for example the one depicted in Fig. A.1. In particular we want to explore the possibility to build an effective model in which the hopping of dipoles as defined in Sec. 2.1.2 is allowed. Such a model will require a second order process in the creation/annihilation operators for bosons. Therefore, as presented in Sec. A.1 the Schrieffer-Wolff transformation turns out to be the perfect mechanism to do it.

First, we need to set the source and target states of the process. They are the Fock states $|i\rangle = |201\rangle$ and $|j\rangle = |120\rangle$, respectively. Here, we are working on a $3/3$ system because it is the minimal system that can have the process we want to describe, though for a B-H system to have dipoles it is enough if we have a $2/2$ system. But for the dipole to be allowed to hop we need at least one more site. Second, we notice that within the possibilities of the single-band model the only way to connect the source and target states is by hopping processes of single particles. Thus There are two intermediate virtual states given by $|k\rangle = |111\rangle$ and $|k\rangle$ = $|210\rangle$ (see Fig. A.1).

We need now to identify the respective energies of the states $|201\rangle$, $|120\rangle$, $|111\rangle$, and $|210\rangle$. Once we have that it is easy to compute the expression in Eq. (A.10) by taking into account that V is the hopping operator given by

$$V = -J \sum_l (a^\dagger_{l+1} a_l + \text{h.c.}) \,. \tag{A.11}$$

It follows that the operator that accounts for the process in Fig. A.1 is

$$O_{\mathrm{SO}} = 2J^2 \left(\frac{1}{F-U} + \frac{1}{F} \right) (a_{l+2}^\dagger a_{l+1} a_l^\dagger a_{l+1} + \mathrm{h.c.}) \,, \tag{A.12}$$

where the coefficients $\frac{2J^2}{F-U}$ and $\frac{2J^2}{F}$ were obtained computing the expression in Eq. (A.10). Interestingly each of the two possible virtual process depicted in Fig. A.1 are represented by combinations of the same creation (anihilation) operators acting on different sites that turn out to be equivallent ones. To see that, let us describe what is happening on each channel of Fig. A.1. If we label the sites by l, $l+1$, and $l+2$, then we are creating two particles in site $l+1$ and anihilating one particle in each site l and $l+2$. The two successive hoppings in top an bottom channels are represented by $a_{l+1}^\dagger a_l a_{l+1}^\dagger a_{l+2}$ and $a_{l+1}^\dagger a_{l+2} a_{l+1}^\dagger a_l$, respecivley. These two operators are equivallent ones due to the commutation relations for bosonic operators.

A.1.2 Application of the SWT to the two-band Bose-Hubbard model

As described in Sec. A.1, we need to identify the intermediate states that are part of the full transit we want to perform. First, the initial and target states of our transit are the Fock states $|i\rangle = |11;00\rangle$ and $|j\rangle = |10;10\rangle$. This final state was chosen based on the results obtained in Sec. 3.3 where we could observe that once we are in such a state the dissipation leads us to the desired superposition.

It is enough for our study to work with a system of two particles in two wells (2/2). In that case, as we saw in Chap. 3 the Fock space of our problem has only 10 elements. It turns out that from all the possible eight intermediate states there is only one such state that will allow us to complete the desired transit. We are talking about $|k\rangle = |20;00\rangle$ and the second order processes behind this transit consist of a hopping and a successive action of the inter-band coupling as depicted in Fig. A.2.

The Hamiltonian of our problem is given by

$$H = H_{B-H}^a + H_{B-H}^b + 2\pi F C_0 \sum_l (a_l^\dagger b_l + b_l^\dagger a_l) \,, \tag{A.13}$$

where $H_{B-H}^{a,b}$ stands for the single-band Bose-Hubbard Hamiltonian for each of the Bloch bands, and the extra term is the well known dipole coupling. In order to apply the Schrieffer-Wolff transformationwe define V as,

$$V = J_a \sum_l (a_{l+1}^\dagger a_l + \mathrm{h.c.}) + 2\pi F C_0 \sum_l (a_l^\dagger b_l + \mathrm{h.c.}) \,, \tag{A.14}$$

the hopping in the lower band and the inter-band coupling. Once we have settled that we can easily compute the value in Eq. (A.10). Thus, the operator that accounts for the processes in Fig. A.2 is

$$\begin{aligned} O_{\mathrm{SO}} &= \left(\frac{1}{2\pi F - W_a/2} - \frac{1}{W_a/2 - \Delta_g} \right) (2\pi F C_0 J_a)(b_l^\dagger a_l a_l^\dagger a_{l+1} + \mathrm{h.c.}) \\ &= U_{\mathrm{SO}}(b_l^\dagger a_{l+1} + \mathrm{h.c.}) + U_{\mathrm{SO}}(b_l^\dagger a_{l+1} + \mathrm{h.c.}) n_l^a \,, \end{aligned} \tag{A.15}$$

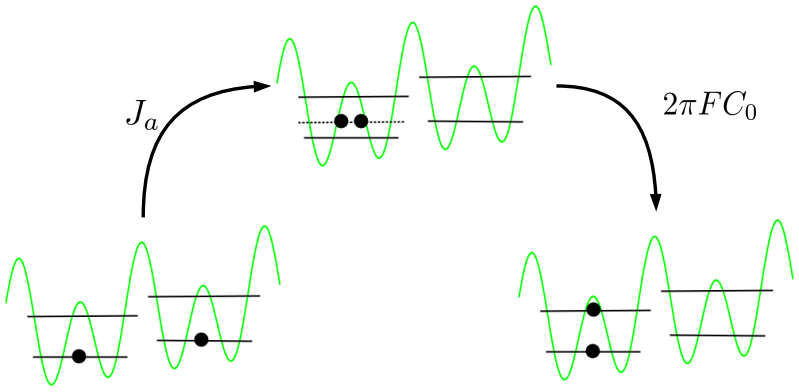

Figure A.2: Schematic representation of the second order processes that take place in our system. We start with a state $|11;00\rangle$, then a hopping carry us to the intermediate state $|20;00\rangle$, and finally the inter-band coupling makes us end in the desired state $|10;10\rangle$.

where we have included the hermitian conjugate to guarantee conservation of energy, and $U_{\mathrm{SO}} = \left(\frac{1}{2\pi F - W_a/2} - \frac{1}{W_a/2 - \Delta_g}\right)$. The parameter we have defined as U_{SO} is the respective form in terms of the Bose-Hubbard parameters for the value G_x introduced along with the Hamiltonian we have presented in Chap. 3.

Appendix B

Miscellaneous results regarding the parametric evolution

We have splitted this section in two main parts. First, results with the intra-site coupling (Sec. B.1), and second, results with the inter-site coupling (Sec. B.2). Why two different kind of couplings? The answer is simple, there are two different ways of introducing an inter-band coupling in the two-band Bose-Hubbard Hamiltonian. This coupling can connect the two bands by means of energy levels in the same site, just like the one we present in Chap. 3. Also, the coupling can connect the bands by means of energy levels in next neighboring sites. The last coupling is not an intuitive one, but we have to consider it since it is the one that the Schrieffer-Wolff transformation gives us (see Eq. (A.15)).

Along this appendix we preserve the same color code for figures and tables when labeling curves and states, respectively, for each pair of figure-table that stands for the results of the evolution with the same initial state. In addition, we have included in the tables the maximum probability of participation for the states that take part in the dynamics. We shall notice that such probabilities does not happen for the same value of α for all the states.

B.1 Results with the intra-site coupling

As stated at the end of Sec. 3.4 we have worked the dynamical evolution of our system for each of the α values in the proper mesh for two other different initial conditions. First we use $|2020;0000\rangle$. The results for this initial condition can be seen in top panel of Fig. B.1. One interesting aspect of the results is the behavior of the states that get excited in the diabatic regime. Even when we are doing a fast sweep the system seems to have enough time to coupled some states to the initial one, and this coupling introduces oscillations among the participating states.

We have found that not even in the adiabatic regime the system is able to end in a superposition of states with alternating site population like $|1010;0101\rangle$ and $|0101;1010\rangle$, and the only one with equal population of both bands $|1010;1010\rangle$ is being mixed in the diabatic regime. In top panel of Table B.1 we present the corresponding states with their respective maximum participation probability labeled by their position in the Fock basis. These probabilities are shown in top panel

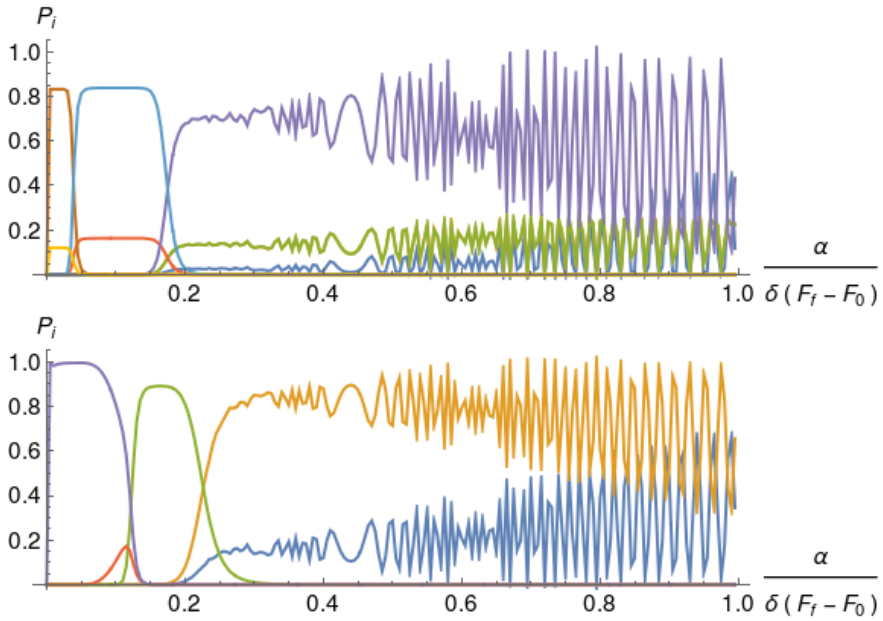

Figure B.1: Top: states participating in the navigation process for the initial state $|2020;0000\rangle$. Bottom: states participating in the navigation process for the initial state $|0202;0000\rangle$. In both cases there are three different dynamical regimes, adiabatic, non-adiabatic, and diabatic just as for the $2/2$ system.

Table B.1: Dynamical states for the initial condition $|2020;0000\rangle$ (top) and $|0202;0000\rangle$ (bottom). We tabulate the probability P_i (on the left of each column) of finding the i-th state (on the right of each column) in the final state for the diabatic, non-adiabatic and adiabatic regimes.

Diabatic regime		Non-adiabatic regime		Adiabatic regime	
$P_{10} = 0.4375$	$\|2020;0000\rangle$	$P_{148} = 0.1630$	$\|0200;1010\rangle$	$P_{233} = 0.8308$	$\|0100;2010\rangle$
$P_{43} = 0.2519$	$\|1020;1000\rangle$	$P_{237} = 0.8370$	$\|0100;1110\rangle$	$P_{245} = 0.1201$	$\|0100;1020\rangle$
$P_{80} = 0.2518$	$\|2010;0010\rangle$				
$P_{149} = 0.9986$	$\|1010;1010\rangle$				
Diabatic regime		**Non-adiabatic regime**		**Adiabatic regime**	
$P_{28} = 0.6621$	$\|0202;0000\rangle$	$P_{73} = 0.9993$	$\|0102;0100\rangle$	$P_{251} = 0.9948$	$\|0001;0120\rangle$
		$P_{165} = 0.8911$	$\|0002;0110\rangle$		
		$P_{242} = 0.1719$	$\|0010;0210\rangle$		

of Fig. B.1 using the same color code of the previous table. States sharing the same color appear as equally weighted superpositions.

Then we use the state $|0202;0000\rangle$ as initial condition. Here, the states that are excited as a consequence of the navigation present, in all the three regimes, a similar behavior of those of the $|2020;0000\rangle$ initial condition (see Fig. B.1 (top)). In bottom panel of Table B.1 we present the respective states with their respective maximum participation probability labeled by their position in the Fock basis. We did not find in this case any equally weighted superposition of any kind. The only state with equal population of both bands $|0002;0110\rangle$ participating in the dynamics is in the non-adiabatic regime being part of a superposition.

B.2 Results with the inter-site coupling

In App. A we found that the second order process we were after, appears as a correction to the Hamiltonian as a higher order term in the creation/annihilation operators for both Bloch bands. The two single particle energy levels in different bands that are being connected by this term are from next neighboring sites, hence, we talk of an inter-site coupling.

B.2.1 Results for the 2/2 system

Following the procedure depicted in Sec. 3.4 we performed the same steps and calculations for the $2/2$ system, but now with a Hamiltonian which has an inter-site coupling rather than an intra-site coupling.

First, we look at the long time average population of the second band as a function of the Stark force (see left panel of Fig. B.2). We found signatures of resonant behavior around three different points, and it is of special interest for our study the one corresponding to the first order resonance, featuring the largest resonant response.

Then, we settled up our force functions to perform parametric evolution around this first order resonance. We compute the time evolution of our system with the initial condition of $|11;00\rangle$ and investigate the states that got excited for different α values. The results can be seen in the right panel of Fig. B.2. We found that in the adibatic and non-adiabatic regimes the only state that is excited by the time evolution is $|01;10\rangle$, and for the diabatic regime we end up in the state $|11;00\rangle$.

B.2.2 Results for the 4/4 system

Similarly to the previous section on the $2/2$ system, here we focus our attention on the adiabatic regime of the $4/4$ system and define our Stark force such that we evolve around the first order resonance. We compute the time evolution of our system for different α values. This calculation was done for three different initial conditions given by $|1111;000\rangle$, $|2020;0000\rangle$, and $|0202;0000\rangle$.

First, for $|1111;000\rangle$ there are only five states that take part in the evolution (see Fig. B.3 and Table B.2). Now there are no equally weighted superpositions in any of the three dynamical regimes. There is only one state with equal population of the bands, located inside the non-adiabatic regime, given by $|0011;1100\rangle$.

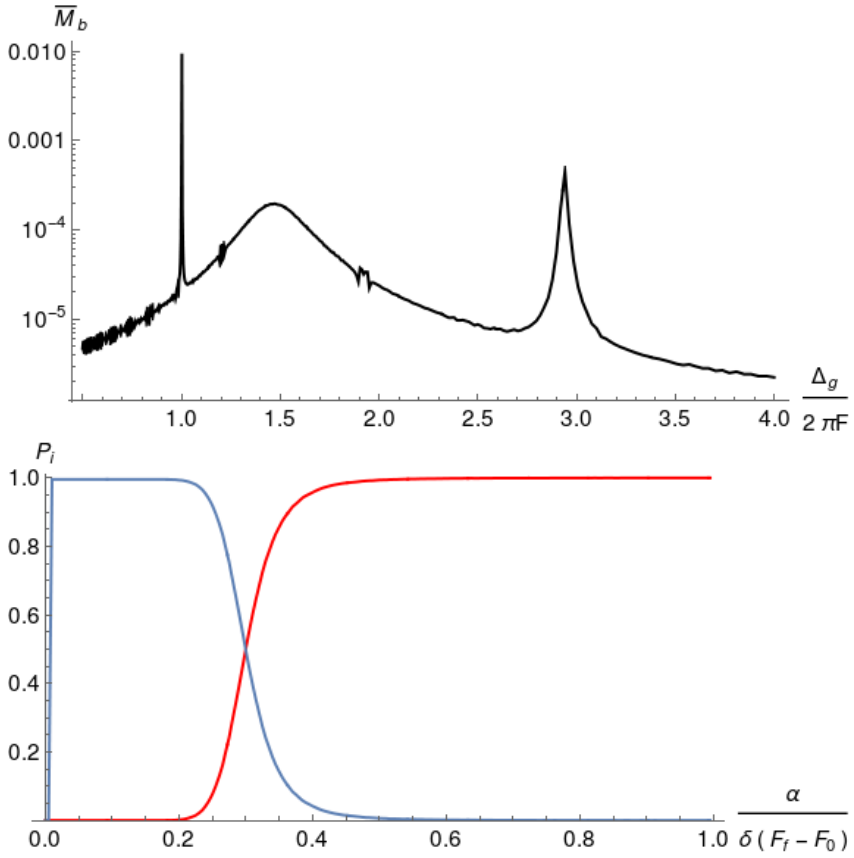

Figure B.2: Top: long time average of the population in the second band as a function of the external force tilting the system. We observe clear signatures of resonant behavior around three specific values of $\frac{\Delta_g}{2\pi F} = \{1, 1.5, 3\}$. We have interest in the first one, being this the respective value of the first order resonance. Bottom: different states participating in the time evolution for different values of α. There is only one state $|01;10\rangle$ that is excited in both the adiabatic and non-adiabatic regime, and only one in the diabatic regime $|11;00\rangle$.

Second, for the $|2020;0000\rangle$ there are only four different states participating in the dynamics, see Fig. B.4 and Table B.3. Now in the diabatic regime we have presence of the initial state $|2020;0000\rangle$ and an additional state $|2010;0100\rangle$. Thus even when we go fast through the AC the system has enough time to couple the initial state to some other state. However, as we go deep in the diabatic regime we recover the normal behavior that is expected for this regime, ending completely in the initial state. Interestingly the adiabatic regime and the non-adiabatic regime have presence of the same two states, $|0100;2100\rangle$ and $|0010;1200\rangle$.

Third, for the initial condition $|0202;0000\rangle$ there are only four dynamical states, see Fig. B.5 and Table B.4. There is one state in the adiabatic regime, $|0010;1200\rangle$. There is one state in the non-adiabatic regime given by $|0002;1100\rangle$. And the diabatic regime has two states. Initially there is a sub-regime within the diabatic one where the state $|0102;1000\rangle$ dominates the dynamics, and later, deep in the diabatic regime, there is a sub-regime where the initial state $|1111;0000\rangle$ dominates the dynamics.

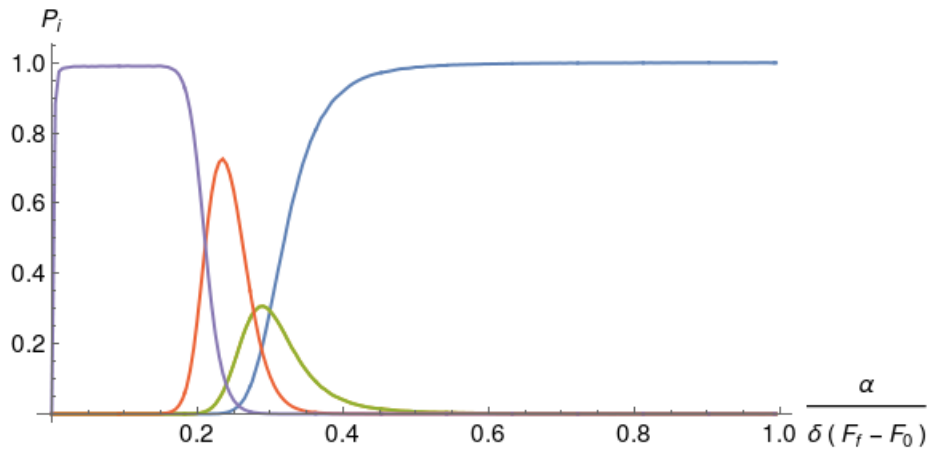

Figure B.3: Different states participating in the navigation process for the initial state $|1111;0000\rangle$. There are three different dynamical regimes, adiabatic, non-adiabatic, and adiabatic just as for the $2/2$ system.

Table B.2: Dynamical states for the initial condition $|1111;0000\rangle$ with Inter-site coupling. We tabulate the maximum probability P_i (on the left of each column) of finding the i-th state (on the right of each column) in the final state for the diabatic, non-adiabatic and adiabatic regimes.

Diabatic regime		Non-adiabatic regime		Adiabatic regime	
$P_{21} = 0.9995$	$\|1111;0000\rangle$	$P_{50} = 0.3071$	$\|0111;1000\rangle$	$P_{226} = 0.9902$	$\|0010;1200\rangle$
		$P_{69} = 0.3069$	$\|1011;0100\rangle$		
		$P_{134} = 0.7257$	$\|0011;1100\rangle$		

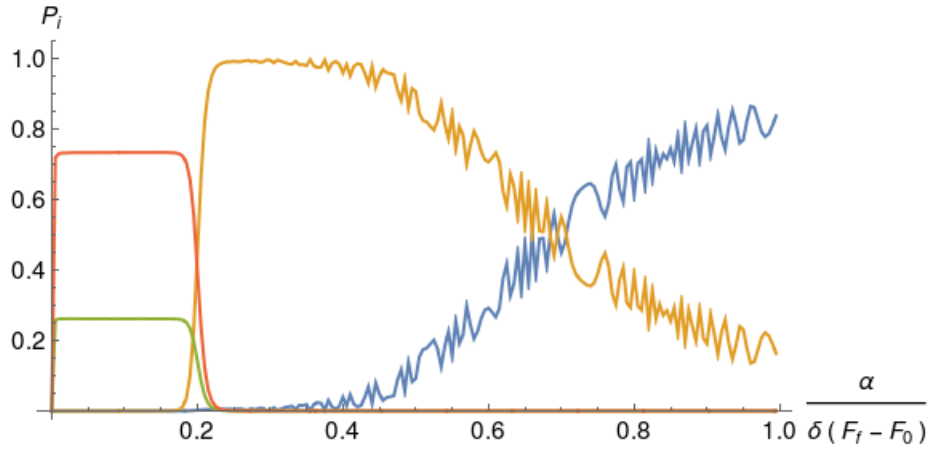

Figure B.4: Different states participating in the parametric evolution for the initial state $|2020;0000\rangle$. There are three different dynamical regimes, adiabatic, non-adiabatic, and diabatic.

Table B.3: Dynamical states for the initial condition $|2020;0000\rangle$ with inter-site coupling. We tabulate the maximum probability P_i (on the left of each column) of finding the i-th state (on the right of each column) in the final state for the diabatic, non-adiabatic and adiabatic regimes.

Diabatic regime		Non-adiabatic regime		Adiabatic regime	
$P_{10} = 0.8639$	$\|2020;0000\rangle$	$P_{221} = 0.2613$	$\|0100;2100\rangle$	$P_{221} = 0.2613$	$\|0100;2100\rangle$
$P_{60} = 0.9959$	$\|2010;0100\rangle$	$P_{226} = 0.7329$	$\|0010;1200\rangle$	$P_{226} = 0.7329$	$\|0010;1200\rangle$

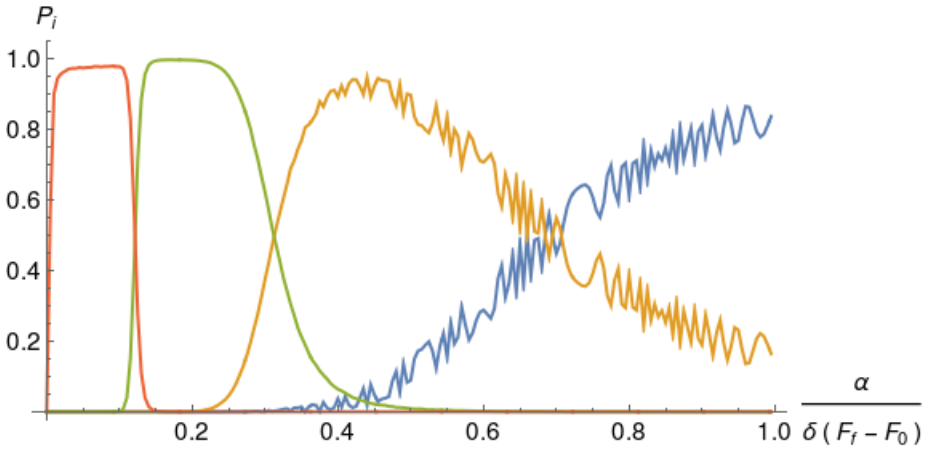

Figure B.5: Different states participating in the parametric evolution for the initial state $|0202;0000\rangle$. There are three different dynamical regimes, adiabatic, non-adiabatic, and diabatic.

Table B.4: Dynamical states for the initial condition $|0202;0000\rangle$ with inter-site coupling. We tabulate the maximum probability P_i (on the left of each column) of finding the i-th state (on the right of each column) in the final state for the diabatic, non-adiabatic and adiabatic regimes.

Diabatic regime		Non-adiabatic regime		Adiabatic regime	
$P_{28} = 0.8627$	$\|0202;0000\rangle$	$P_{135} = 0.9943$	$\|0002;1100\rangle$	$P_{226} = 0.9767$	$\|0010;1200\rangle$
$P_{53} = 0.9444$	$\|0102;1000\rangle$				

Appendix C

Interference time and a dipole in the middle of the lattice

This brief appendix is devoted to two issues. We expand on the results presented in Sec. 2.2.4 about the length of the interference patterns when we increase the size of the system. We also present a different example of the time evolution and behavior a dipole can have when it is placed in a different position than the edge of the chain.

C.1 Interference time

In Sec. 2.2.4 we presented the main result for the interference time which exhibits an exponential behavior with the size of the system. This conclusion was drawn with the help of the effective model, and we could see that the results in the whole model and the effective one match pretty well.

However, there is still a question for which we have not given an answer yet. Why did we have to study the case of even lattice size apart from those of odd size? From Fig. 2.7 it is clear that interference in odd sized systems last longer that in even sized systems. Such a differentiation can be attributed to the process by means of which the initial excitation (the dipole) delocalizes on the lattice space and later reconstruct its initial configuration. This can be seen in the IPR-like functional as defined in Sec. 2.2.3 which is plotted in Fig. C.1 (red curves). More precisely, we observe a series of decreasing peaks at short times characterizing the delocalization process of the wave packet, followed by a region of interference. For even number of sites the relocalization occurs after this region of interference. For odd number of sites the situation is different. After the first region of interference the wave packet behavior alternates partial revivals of the initial configuration with interference. Only at large times the initial condition is recovered.

In left part of Fig. C.1 we present two examples of the time evolution of B-H systems with 8 and 12 sites, respectively. We see the appearance of the interference and how it clearly increases as we scale the number of lattice sites. The interference time we are reporting was taken to be the time between the peak of the IPR at zero and the highest value to the IPR following the previous one. In right panels of Fig. C.1 we present the same study but for systems with odd size: 9 and

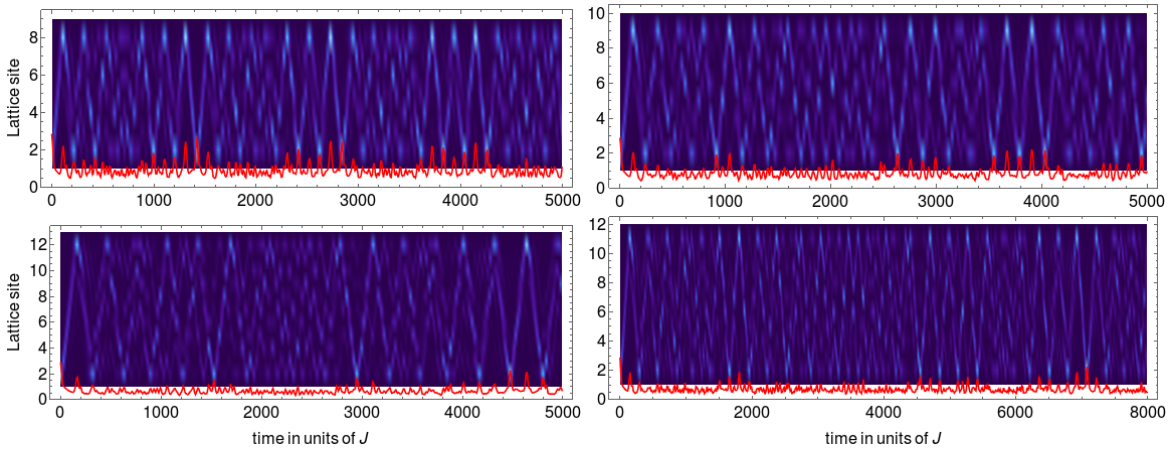

Figure C.1: Time evolution of the population in each lattice site within the effective XXZ-chain model representing a B-H system of eight (top-left), twelve (bottom-left), nine (top-right) and eleven (bottom-right) sites. For even number of sites the reconstruction of the wave packet occurs after the first interference process, while for odd number of sites there is a large region of interference and partial revivals before the initial wave packet is recovered.

11 sites, respectively.

Although the differentiation between odd sized and even sized systems is necessary from the point of view of the interference time. The neat result here is that this differentiation is only a finite size effect. We saw the evidence supporting this in last part of Sec. 2.2.4.

C.2 A dipole in the middle of the lattice

In Sec. 1.5 we present how it is possible to connect the single-band Bose-Hubbard model with the Heisenberg XXZ-model by means of tilting the lattice and a proper second order tunneling process. This connection allowed us to interpret the propagation of one single dipole as the propagation of a single spin impurity, in other words as a spin-wave.

So far the results we have presented were for a dipole placed in one edge of the lattice. In general one can think of other configurations. We consider here the special case when the dipole is placed in the middle of the lattice. That is, we choose as initial condition the Fock state $|112011\rangle$. For the sake of shortness we only present the results of its time evolution. We do not include extensive studies of the interference and other parts of the analysis we did in Chap. 2 because they are essencially very similar to the results already presented there.

What would be the evolution of our system with such initial condition? Since we are working in a tilted lattice where the translational invariance has been broken one might think that there is a natural direction for the propagation of excitations. In Fig. C.2 we present the results of the time evolution for the initial condition $|112011\rangle$ for both the full B-H model and the effective model.

The major result that can be seen in Fig. C.2 is that our initial assumption about the time evolution was wrong. That is remarkable, because even though we are in a system where the translational invariance has been broken, excitations, dipoles in our case, undergo a translational

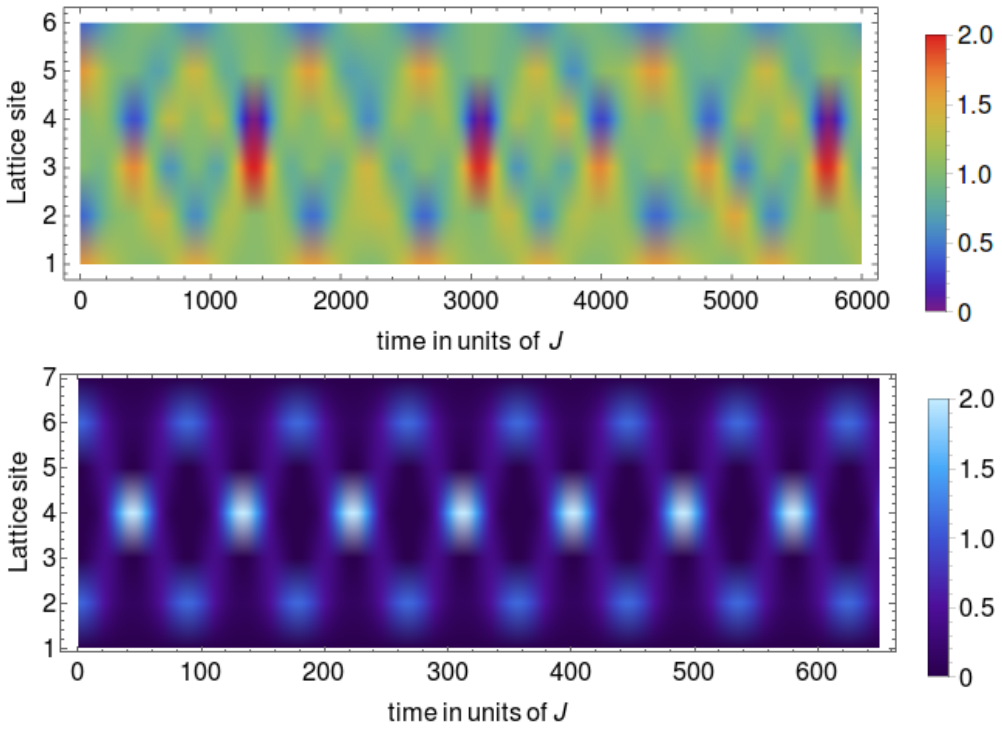

Figure C.2: Top: time evolution of the population for the different lattice sites in the Bose-Hubbard model with initial condition $|112011\rangle$. Blue referes to a vacancy or a holon while red means double population or doublon. Bottom: time evolution of the population of the lattice sites in the case of the effective model for the same initial condition as in the upper part.

invariant lattice and therefore there is no preferred direction of propagation. Also, the dipole propagates as a whole entity and does not split in its individual components, holon propagating in one direction and doublon propagating in the oposite one. Finally, the lower panel of Fig. C.2 we can see that the effective model is a neat representation of the dynamics in the whole B-H system.

Bibliography

[1] C. C. Bradley, C. A. Sackett, and R. G. Hulet. *Bose-Einstein Condensation of Lithium: Observation of Limited Condensate Number*. *Physical Review Letters* **78**(6), 985–989 (1997). DOI: 10.1103/PhysRevLett.78.985.

[2] K. Davis, M. Mewes, M. Andrews, N. van Druten, D. Durfee, D. Kurn, and W. Ketterle. *Bose-Einstein Condensation in a Gas of Sodium Atoms*. *Physical Review Letters* **75**(22), 3969–3973 (1995). DOI: 10.1103/PhysRevLett.75.3969.

[3] M H Anderson, J R Ensher, M R Matthews, C E Wieman, and E A Cornell. *Observation of bose-einstein condensation in a dilute atomic vapor. Science (New York, N.Y.)* **269**(5221), 198–201 (1995). DOI: 10.1126/science.269.5221.198.

[4] Markus Greiner, Olaf Mandel, Tilman Esslinger, Theodor W Hänsch, and Immanuel Bloch. *Quantum phase transition from a superfluid to a Mott insulator in a gas of ultracold atoms. Nature* **415**(6867), 39–44 (2002). DOI: 10.1038/415039a.

[5] Immanuel Bloch, Jean Dalibard, and Wilhelm Zwerger. *Many-body physics with ultracold gases*. *Reviews of Modern Physics* **80**(3), 885–964 (2008). DOI: 10.1103/RevModPhys.80.885.

[6] Immanuel Bloch, Jean Dalibard, and Sylvain Nascimbène. *Quantum simulations with ultracold quantum gases*. *Nature Physics* **8**(4), 267–276 (2012). DOI: 10.1038/nphys2259.

[7] Jonathan Simon, Waseem S Bakr, Ruichao Ma, M Eric Tai, Philipp M Preiss, and Markus Greiner. *Quantum simulation of antiferromagnetic spin chains in an optical lattice. Nature* **472**(7343), 307–12 (2011). DOI: 10.1038/nature09994.

[8] M. Aidelsburger, M. Atala, M. Lohse, J. T. Barreiro, B. Paredes, and I. Bloch. *Realization of the Hofstadter Hamiltonian with Ultracold Atoms in Optical Lattices*. *Physical Review Letters* **111**(18), 185301 (2013). DOI: 10.1103/PhysRevLett.111.185301.

[9] J Struck, C Ölschläger, R Le Targat, P Soltan-Panahi, A Eckardt, M Lewenstein, P Windpassinger, and K Sengstock. *Quantum simulation of frustrated classical magnetism in triangular optical lattices. Science (New York, N.Y.)* **333**(6045), 996–9 (2011). DOI: 10.1126/science.1207239.

[10] Carlos A. Parra-Murillo, Javier Madroñero, and Sandro Wimberger. *Quantum diffusion and thermalization at resonant tunneling*. *Physical Review A* **89**(5), 053610 (2014). DOI: 10.1103/PhysRevA.89.053610.

[11] Michael Lubasch, Florian Mintert, and Sandro Wimberger. *Dynamical enhancement of spatial entanglement in massive particles*. *Physical Review A* **84**(6), 063615 (2011). DOI: 10.1103/PhysRevA.84.063615.

[12] C. Sias, H. Lignier, Y. Singh, A. Zenesini, D. Ciampini, O. Morsch, and E. Arimondo. *Observation of Photon-Assisted Tunneling in Optical Lattices*. *Physical Review Letters* **100**(4), 040404 (2008). DOI: 10.1103/PhysRevLett.100.040404.

[13] C. Sias, A. Zenesini, H. Lignier, S. Wimberger, D. Ciampini, O. Morsch, and E. Arimondo. *Resonantly Enhanced Tunneling of Bose-Einstein Condensates in Periodic Potentials*. *Physical Review Letters* **98**(12), 120403 (2007). DOI: 10.1103/PhysRevLett.98.120403.

[14] Andreas Trabesinger. *Quantum simulation*. *Nature Physics* **8**(4), 263–263 (2012). DOI: 10.1038/nphys2258.

[15] R. Blatt and C. F. Roos. *Quantum simulations with trapped ions*. *Nature Physics* **8**(4), 277–284 (2012). DOI: 10.1038/nphys2252.

[16] Alán Aspuru-Guzik and Philip Walther. *Photonic quantum simulators*. *Nature Physics* **8**(4), 285–291 (2012). DOI: 10.1038/nphys2253.

[17] Andrew A. Houck, Hakan E. Türeci, and Jens Koch. *On-chip quantum simulation with superconducting circuits*. *Nature Physics* **8**(4), 292–299 (2012). DOI: 10.1038/nphys2251.

[18] T.W. Hänsch and A.L. Schawlow. *Cooling of gases by laser radiation*. *Optics Communications* **13**(1), 68–69 (1975). DOI: 10.1016/0030-4018(75)90159-5.

[19] P. D. Lett, W. D. Phillips, S. L. Rolston, C. E. Tanner, R. N. Watts, and C. I. Westbrook. *Optical molasses*. *Journal of the Optical Society of America B* **6**(11), 2084 (1989). DOI: 10.1364/JOSAB.6.002084.

[20] Harold J. Metcalf and Peter van der Straten. *Laser Cooling and Trapping*, volume 9. Springer Science & Business Media (2001).

[21] Wolfgang Ketterle and N.J. Van Druten. *Evaporative Cooling of Trapped Atoms*. *Advances In Atomic, Molecular, and Optical Physics* **37**, 181–236 (1996). DOI: 10.1016/S1049-250X(08)60101-9.

[22] C. J. Pethick and H. Smith. *Bose-Einstein Condensation in Dilute Gases*. Cambridge University Press (2002).

[23] S. Bose. *Plancks Gesetz und Lichtquantenhypotheses. Zeitscrhift für physik* **26**, 178 (1924).

[24] Claude Cohen-Tannoudji, Jacques Dupont-Roc, and Gilbert Grynberg. *Photons and Atoms: Introduction to Quantum Electrodynamics*. Wiley (1997).

[25] Roberto B. Diener, Georgios A. Georgakis, Jianxin Zhong, Mark Raizen, and Qian Niu. *Transition between extended and localized states in a one-dimensional incommensurate optical lattice*. *Physical Review A* **64**(3), 033416 (2001). DOI: 10.1103/PhysRevA.64.033416.

[26] M Glück, Andrey R. Kolovsky, and Hans Jürgen Korsch. *Wannier–Stark resonances in optical and semiconductor superlattices*. *Physics Reports* **366**(3), 103–182 (2002). DOI: 10.1016/S0370-1573(02)00142-4.

[27] Andrey Kolovsky and Andreas Buchleitner. *Floquet-Bloch operator for the Bose-Hubbard model with static field*. *Physical Review E* **68**(5), 056213 (2003). DOI: 10.1103/PhysRevE.68.056213.

[28] C. Zener. *A Theory of the Electrical Breakdown of Solid Dielectrics*. *Proceedings of the Royal Society A: Mathematical, Physical and Engineering Sciences* **145**(855), 523–529 (1934). DOI: 10.1098/rspa.1934.0116.

[29] A. Zenesini, H. Lignier, G. Tayebirad, J. Radogostowicz, D. Ciampini, R. Mannella, S. Wimberger, O. Morsch, and E. Arimondo. *Time-Resolved Measurement of Landau-Zener Tunneling in Periodic Potentials*. *Physical Review Letters* **103**(9), 090403 (2009). DOI: 10.1103/PhysRevLett.103.090403.

[30] Andrea Tomadin. *Quantum Chaos with Ultra Cold Atoms in Optical Lattices*. Master's thesis, University of Pisa (2006).

[31] A. Fetter and J. Walecka. *Quantum Theory of Many-Particle Systems.* McGraw-Hill, New York (1971).

[32] M. Olshanii. *Atomic Scattering in the Presence of an External Confinement and a Gas of Impenetrable Bosons*. *Physical Review Letters* **81**(5), 938–941 (1998). DOI: 10.1103/PhysRevLett.81.938.

[33] Neil W. Ashcroft and N. David Mermin. *Solid State Physics*. Holt, Rinehart and Winston (1976).

[34] W. Kohn. *Construction of Wannier Functions and Applications to Energy Bands*. *Physical Review B* **7**(10), 4388–4398 (1973). DOI: 10.1103/PhysRevB.7.4388.

[35] Carlos A. Parra-Murillo. *Many-Body Dynamics of Ultra Cold Atoms in Optical Lattices*. Ph.d. thesis, Heidelberg University (2013).

[36] Patrick Plötz. *Complex Dynamics of Ultra Cold Atoms*. Ph.d. thesis, Heidelberg University (2010).

[37] Hans-Jürgen Mikeska and Alexei K. Kolezhuk. *One-dimensional magnetism*. In Ulrich Schollwöck, Johannes Richter, Damian J. J. Farnell, and Raymod F. Bishop, editors, *Quantum Magnetism*, volume 645 of *Lecture Notes in Physics*, pages 1–88. Springer Berlin Heidelberg, Berlin, Heidelberg (2004).

[38] A. Langari. *Phase diagram of the antiferromagnetic XXZ model in the presence of an external magnetic field*. *Physical Review B* **58**(21), 14467–14475 (1998). DOI: 10.1103/PhysRevB.58.14467.

[39] Subir Sachdev, K. Sengupta, and S. Girvin. *Mott insulators in strong electric fields*. *Physical Review B* **66**(7), 075128 (2002). DOI: 10.1103/PhysRevB.66.075128.

[40] Andrey Kolovsky. *Bloch oscillations in the Mott-insulator regime*. *Physical Review A* **70**(1), 015604 (2004). DOI: 10.1103/PhysRevA.70.015604.

[41] Ian B Spielman. *Atomic physics: A route to quantum magnetism. Nature* **472**(7343), 301–2 (2011). DOI: 10.1038/nature10101.

[42] A. A. Ovchinnikov, D. V. Dmitriev, V. Ya. Krivnov, and V. O. Cheranovskii. *Antiferromagnetic Ising chain in a mixed transverse and longitudinal magnetic field*. *Physical Review B* **68**(21), 214406 (2003). DOI: 10.1103/PhysRevB.68.214406.

[43] Subir Sachdev. *Quantum Phase Transitions*. Cambridge University Press, 2nd edition (2011).

[44] F. Meinert, M. J. Mark, E. Kirilov, K. Lauber, P. Weinmann, A. J. Daley, and H.-C. Nägerl. *Quantum Quench in an Atomic One-Dimensional Ising Chain*. *Physical Review Letters* **111**(5), 053003 (2013). DOI: 10.1103/PhysRevLett.111.053003.

[45] Michael V Berry, I Marzoli, and W Schleich. *Quantum carpets, carpets of light*. *Physics World* **June 2001** (2001).

[46] J. Schrieffer and P. Wolff. *Relation between the Anderson and Kondo Hamiltonians*. *Physical Review* **149**(2), 491–492 (1966). DOI: 10.1103/PhysRev.149.491.

[47] Raymond Chan and Miklós Gulácsi. *The exact Schrieffer–Wolff transformation*. *Philosophical Magazine* **84**(12), 1265–1279 (2004). DOI: 10.1080/14786430310001653107.

[48] Andrea Tomadin, Riccardo Mannella, and Sandro Wimberger. *Many-Body Interband Tunneling as a Witness of Complex Dynamics in the Bose-Hubbard Model*. *Physical Review Letters* **98**(13), 130402 (2007). DOI: 10.1103/PhysRevLett.98.130402.

[49] Andrea Tomadin, Riccardo Mannella, and Sandro Wimberger. *Many-body Landau-Zener tunneling in the Bose-Hubbard model*. *Physical Review A* **77**(1), 013606 (2008). DOI: 10.1103/PhysRevA.77.013606.

[50] Alessandro Zenesini, Hans Lignier, Donatella Ciampini, Oliver Morsch, and Ennio Arimondo. *Coherent Control of Dressed Matter Waves*. *Physical Review Letters* **102**(10), 100403 (2009). DOI: 10.1103/PhysRevLett.102.100403.

[51] H. Lignier, C. Sias, D. Ciampini, Y. Singh, A. Zenesini, O. Morsch, and E. Arimondo. *Dynamical Control of Matter-Wave Tunneling in Periodic Potentials*. *Physical Review Letters* **99**(22), 220403 (2007). DOI: 10.1103/PhysRevLett.99.220403.

[52] Carlos A. Parra-Murillo, Javier Madroñero, and Sandro Wimberger. *Two-band Bose-Hubbard model for many-body resonant tunneling in the Wannier-Stark system*. *Physical Review A* **88**(3), 032119 (2013). DOI: 10.1103/PhysRevA.88.032119.

[53] Mark G. Bason, Matthieu Viteau, Nicola Malossi, Paul Huillery, Ennio Arimondo, Donatella Ciampini, Rosario Fazio, Vittorio Giovannetti, Riccardo Mannella, and Oliver Morsch. *High-fidelity quantum driving*. *Nature Physics* **8**(2), 147–152 (2011). DOI: 10.1038/nphys2170.

[54] Shen Shun-Qing. *Topological Insulators - Dirac Equation in Condensed Matters*. Springer-Verlag Berlin Heidelberg, 1st edition (2012).

[55] Sergey Bravyi, David P. DiVincenzo, and Daniel Loss. *Schrieffer–Wolff transformation for quantum many-body systems*. *Annals of Physics* **326**(10), 2793–2826 (2011). DOI: 10.1016/j.aop.2011.06.004.

[56] M. Dalmonte, E. Ercolessi, M. Mattioli, F. Ortolani, and D. Vodola. *Magnetic properties of commensurate Bose-Bose mixtures in one-dimensional optical lattices*. *The European Physical Journal Special Topics* **217**(1), 13–27 (2013). DOI: 10.1140/epjst/e2013-01750-2.

[57] T. Barthel, C. Kasztelan, I. P. McCulloch, and U. Schollwöck. *Magnetism, coherent many-particle dynamics, and relaxation with ultracold bosons in optical superlattices*. *Physical Review A* **79**(5), 053627 (2009). DOI: 10.1103/PhysRevA.79.053627.